

2019-01-01

Dimensionality Of Magnetism In Trirutile CoTa₂O₆ And Its Derivatives

Raju Baral

University of Texas at El Paso

Follow this and additional works at: https://digitalcommons.utep.edu/open_etd



Part of the [Condensed Matter Physics Commons](#)

Recommended Citation

Baral, Raju, "Dimensionality Of Magnetism In Trirutile CoTa₂O₆ And Its Derivatives" (2019). *Open Access Theses & Dissertations*. 1972.

https://digitalcommons.utep.edu/open_etd/1972

This is brought to you for free and open access by DigitalCommons@UTEP. It has been accepted for inclusion in Open Access Theses & Dissertations by an authorized administrator of DigitalCommons@UTEP. For more information, please contact lweber@utep.edu.

DIMENSIONALITY OF MAGNETISM IN TRIRUTILE CoTa_2O_6 AND ITS DERIVATIVES

RAJU BARAL

Master's Program in Physics

APPROVED:

Harikrishnan Nair, Ph.D., Chair

Srinivasa Rao Singamaneni, Ph.D.

Sreeprasad Sreenivasan, Ph.D.

Stephen L. Crites, Jr., Ph.D.
Dean of the Graduate School

Copyright ©

by

Raju Baral

2019

DIMNESIONALITY OF MAGNETISM IN TRIRUTILE CoTa_2O_6 AND ITS DERIVATIVES

by

RAJU BARAL, M.S.

THESIS

Presented to the Faculty of the Graduate School of

The University of Texas at El Paso

in Partial Fulfillment

of the Requirements

for the Degree of

MASTER OF SCIENCE

Department of Physics

THE UNIVERSITY OF TEXAS AT EL PASO

August 2019

Acknowledgements

Foremost, I would like to express my sincere gratitude to my advisor **Dr. Harikrishnan Nair** for all the mentorship and opportunity throughout my M.S. in physics. I would also like to acknowledge **Dr. Srinivasa Rao Singamaneni** and **Dr. Sreeprasad Sreenivasan** for agreeing to be a part of this thesis committee. I extend my appreciation to the collaboration performed by **Dr. Tom Heitman** at University of Missouri Research Reactor (MURR) and **Prof. A. M. Strydom**, University of Johannesburg. I would also like to acknowledge **Dr. S. R. Singamaneni** for the laboratory access and use of equipment. I would also want to recognize **Mr. Hector S Fierro** for helping me with data. Similarly, I would like to thank **Dr. Alejandro Metta** and **Dr. Michael Lyubchenko**, the University of Texas at El Paso, for their help and support while operating the powder X-ray diffractometers. Finally, I would like to thank my family and friends for constant support and helpful discussion.

Abstract

In this thesis, we addressed the question of low dimensionality of trirutile compound CoTa_2O_6 and studied how the low dimensionality evolved with doping of Mg on Co-site. In order to study low dimensionality in CoTa_2O_6 and its derivative compounds $\text{Co}_{1-x}\text{Mg}_x\text{Ta}_2\text{O}_6$ ($x = 0.1, 0.3, 0.5, 0.7$, and 1), we used different techniques: X-ray diffraction, magnetic susceptibility, magnetization, specific heat and elastic neutron diffraction. We have addressed the question of low dimensional magnetism of CoTa_2O_6 by preparing phase-pure samples of the compound. In CoTa_2O_6 a broad feature is observed in magnetic susceptibility at 10 K and an antiferromagnetic phase transition is confirmed to occur at 6.2 K through magnetization, specific heat and neutron diffraction. It is noted that the transition peak at 6.2 K in the parent compound is robust up to 7 T and corresponds to an antiferromagnetic transition. With the addition of Mg, the peak at the magnetic transition is suppressed. Significant short-range spin fluctuations are present in CoTa_2O_6 as evidenced through specific heat analysis. The analysis of magnetic susceptibility combined with neutron diffraction data points towards a quasi-low-dimensional magnetic structure in CoTa_2O_6 which is suppressed with the addition of non-magnetic atom due to dilution of interaction between Co-atoms. $\text{Co}_{1-x}\text{Mg}_x\text{Ta}_2\text{O}_6$ with $x > 0.5$ show slight enhancement in ferromagnetism. Structural analysis using X-ray and neutron diffraction data shows anomalies in the lattice parameters corresponding to $x = 0.5$. Future studies will address the role of structure in observed magnetic features and the magnetic excitations in this trirutile compound series.

Table of Contents

Acknowledgements	v
Abstract	vi
Table of Contents	vii
List of Tables	ix
List of Figures	x
Chapter 1: Introduction	1
Chapter 2: Theoretical Background	6
2.1 Crystal structure	6
2.2 Powder X-ray diffraction (PXRD).....	6
2.2.1 PXRD instrument.....	8
2.3 Elastic neutron diffraction.....	8
2.3.1 Neutron scattering cross-section	10
2.3.2 Scattering cross-section	11
2.3.2 Coherent and incoherent neutron scattering	12
2.3.3 Magnetic scattering.....	12
2.3.4 Diffracted neutrons from ideal polycrystalline material	14
2.4 Rietveld analysis	15
2.5 Magnetic properties	17
2.5.1 Magnetic interaction	17
2.5.2 Antiferromagnetism and ferromagnetism	18
2.5.3 Magnetic susceptibility	19
2.5.4 Curie-Weiss law.....	19
2.5.5 Spin chains	20
2.5.6 Two-dimensional magnetism.....	20
2.6 Specific heat capacity of a crystalline solid.....	21
2.6.1 Einstein theory of specific heat of a solid.....	21
2.6.2 Debye theory of specific heat of a solid.....	22

Chapter 3: Synthesis and Magnetic Properties of $\text{Co}_{1-x}\text{Mg}_x\text{Ta}_2\text{O}_6$	23
3.1 Polycrystalline synthesis	23
3.2 Characterization of powder x-ray diffraction data	23
3.2 Characterization of magnetization data	25
3.3 Characterization using Curie-Weiss fit and low dimensional models	26
Chapter 4 Neutron Diffraction and Specific Heat of $\text{Co}_{1-x}\text{Mg}_x\text{Ta}_2\text{O}_6$	31
4.1 Neutron powder diffraction	31
4.2 Specific heat	35
Conclusion	38
References	40
Vita	44

List of Tables

Table I: Energy and wavelength of cold, thermal and hot neutrons	11
Table I: Lattice parameters, goodness of fit and volume of unit cell for $\text{Co}_{1-x}\text{Mg}_x\text{Ta}_2\text{O}_6$, $x = 0, 0.3, 0.7$ and 1 respectively. Fractional coordinates of atoms in the CoTa_2O_6 structure is shown.	29
Table II: Effective paramagnetic moment (μ_{eff}), Curie-Weiss temperature (θ_p), maximum magnetic moment (M_{max}), Lande g-factor, and Ising and Bonner-Fisher fit exchange parameter J_{nnI} (K) and J_{nnBF} (K) are shown in the table.	32
Table III: The atomic position and lattice parameters for the composition $x = 0, 0.3$, and 0.7 at temperature 295 K.....	38
Table IV: Bond distance and bond angles for CoTa_2O_6	39
Table IV: The parameters exacted from the analysis of low temperature specific heat of $\text{Co}_{1-x}\text{Mg}_x\text{Ta}_2\text{O}_6$	44

List of Figures

Figure 1.1 (Left) The crystal structure of CoTa_2O_6 , showing the CoO_6 and TaO_6 octahedra in blue and gray colour, respectively. The oxygen atoms that form the octahedra are shown as red spheres, (Right) Represents the square planar structure of Co magnetic lattice.....	2
Figure 1.2: (Left) The specific heat of CuSb_2O_6 , NiTa_2O_6 and CoSb_2O_6 were seen to display anisotropic effects in the presence of external magnetic field. (Right) A single crystal of CoTa_2O_6 was demonstrated as displaying optical dichroism	3
Figure 1.3: The magnetocaloric effect observed in CoTa_2O_6 and FeTa_2O_6 . Note that this is an anisotropic effect observed due to magnetic field being applied along different crystallographic directions.....	4
Figure 2.1: Seven different type of unit cell	7
Figure 2.2: Represents the geometrical figure of Bragg's law	9
Figure 2.3: This is the architecture diagram of the reactor and instrumental beamline in MURR (Missouri University Research Reactor).....	10
Figure 2.4: Geometrical figure of neutron scattering cross-section.....	12
Figure 2.5: 2D figure of diffraction of neutrons from parallel planes.	16
Figure 2.6: Plot between $1/\chi$ and Temperature (K) for various substance.....	23
Figure 2.6: Normalized specific heat plotted as a function of normalized temperature (normalized with respect to Debye temperature, T_D) for both Einstein and Debye Models.....	26
Figure 3.1: (a-d) The PXRD patterns for $\text{Co}_{1-x}\text{Mg}_x\text{Ta}_2\text{O}_6$ ($x = 0, 0.3, 0.7$ and 1) compositions. Figure 3.1 (e) and (f) represents the variation of lattice parameters with x . Figure (g) show the structural diagram of MgTa_2O_6	28
Figure 3.2: (a) The magnetization vs Temperature curve of CoTa_2O_6 in ZFC and FC protocols at $H_{app} = 1000$ Oe. The black marker shows the paramagnetic response of MgTa_2O_6 which is also represented in the same graph. (b) The ZFC and FC plots of at $H_{app} = 100$ Oe of $x = 0.1$ which showing a bifurcation at 30 K. The inserted graph of dM/dT show three anomalies in the case of $x = 0.1$. (c) An enhancement in magnetism are observed for $x = 0.5$, and 0.7 at low temperature. The inserted graph shows the FC curve of $x = 0.1$ at $H_{app} = 1000$ Oe.....	31
Figure 3.3. The magnetic susceptibility of $\text{Co}_{1-x}\text{Mg}_x\text{Ta}_2\text{O}_6$ compounds plotted in semi-log axis ($x = 0, 0.1$, and 0.7). The magnetic susceptibility data are fitted using Bonner-Fisher model which is represented by pink solid line and Ising model fit is shown by black solid line. The figures (a), (b), and (c) represents cases for $x = 0, 0.1$, and 0.7 respectively.	35
Figure 3.4: (a) The magnetization isotherm, $M(H)$, of CoTa_2O_6 at 2 K, 10 K, and 300 K. The insert graph shows the derivative, which reveals the field-induced transition at 2 T and 5 T. (b) shows the $M(H)$ of $x = 0.1$ at 2 K, 10 K, and 300 K. The insert graph shows a field induced transition present at 1 T at 2 K. (c) shows the $M(H)$ of $x = 0.3, 0.5$, and 0.7 at 2 K. Field-induced transitions are absent for these compositions.....	36
Figure 4.1: The neutron diffraction pattern for $x = 0, 0.3$, and 0.7 at $T = 295$ K.....	38
Figure 4.2: The neutron powder diffraction patterns obtained for $x = 0.1$ and 0.7 at 5 K are presented in Figure (c) and (d) respectively. The low-angle region of the pattern is shown magnified in (c) to clearly show that the magnetic Bragg peaks are absent even with Mg-dilution of 10%.....	41
Figure 4.3: (a) Represents specific heat capacity for $x = 0$ at 0 T, 5 T, and 7 T. Cp of $x = 1$ so shown in same figure with pink color at 0 T, for comparison. The insert graph represents dC_p/dT	

for $x = 0.1$. Figure (b) represents the specific heat capacity for $x = 0, 0.1, 0.3, 0.5, 0.7$, and 1 at 0 T and the insert graph show the C_p of $x = 0.5$ at 0 T and 7 T. Figure (c) represents Ising fit (red solid line) of magnetic specific heat for $x = 0$, in zero field. 43

Chapter 1: Introduction

Research interest in low dimensional magnetic systems is mainly due to the fact that they provide unique possibilities to realize novel magnetic ground states, magnetic excitations, possible new phases of magnetic matter incorporating the interplay of quantum and thermal fluctuations. The magnetic properties of low-dimensional spin systems are strongly dependent on S (spin) of the electron as well as on the existence of single-ion anisotropy, along with the physics brought about by dimensionality of the crystal structure. Control of magnetic order in low-dimensional systems can be important milestone for the nanoelectronics and spintronics. It is difficult to realize long-range magnetic order in low dimensional bulk magnetic systems as it is suppressed by the thermal fluctuation. The Mermin Wagner theorem prohibits the formation of a long-range order in bulk spin systems of reduced dimensionality [1]. There are several 1D and 2D spin systems that are interesting from the perspective of low-dimensionality. In the present thesis, we discuss the physics of a class of compounds called trirutiles of general formula MTa_2O_6 (M = transition metal) where the lattice formed by M can be treated as a square net of spins. The M lattice could also be perceived as a chain of spins aligned along a certain crystallographic axis. The trirutile structure of MTa_2O_6 is derived from the rutile (TiO_2) structure. In rutile structure, each cation, Ti^{+} , is surrounded by 6 oxygen ions, O^{2-} , which forms an octahedral environment. The metal cation in a trirutile has the same basic structure as rutile, but the cations will order in such a way to triple the c -axis. Trirutile compounds crystallize in the space group $P4_2/mnm$, space group number 136 [2]. Since the present thesis deals with the trirutile $CoTa_2O_6$, a schematic of the crystal structure is presented in Figure 1.1. In the figure, the crystal structure composed of CoO_6 and TaO_6 octahedra are shown in blue and grey colored

octahedra. The low dimensional nature (in this case, 2D) of the Co network of spins is presented in the figure where the square net of Co atoms are shown.

Some of the earliest studies on CoTa_2O_6 and related MTa_2O_6 ($M = \text{Co}, \text{Ni}, \text{Fe}$) investigated the specific heat and approximated it to the theoretical case of Ising spins on a square net [3]. These works identified an antiferromagnetic transition (T_N) at 6.67 K for CoTa_2O_6 . As a comparison, the T_N for FeTa_2O_6 was 8.1 K. The specific heat of MTa_2O_6 were analyzed in terms of the Ising square net and exchange constant (J) were determined. This early work itself had identified the presence of short-range spin fluctuations, by analyzing the magnetic entropy in the specific heat, present at temperatures greater than the transition temperatures. The work by Kremer *et al* [3] attains importance as it corrected an error in the previous work on MTa_2O_6 where the transition temperature of CoTa_2O_6 was wrongly estimated as at 35 K [4].

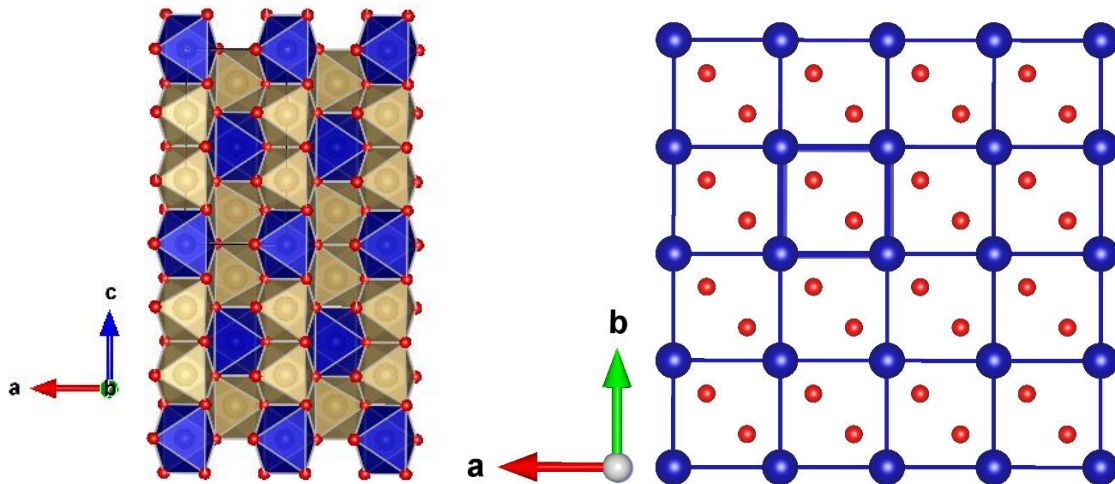


Figure 1.1 (Left) The crystal structure of CoTa_2O_6 , showing the CoO_6 and TaO_6 octahedra in blue and gray colour, respectively. The oxygen atoms that form the octahedra are shown as red spheres, (Right) Represents the square planar structure of Co magnetic lattice. The Co atoms are shown as blue spheres. The structure diagrams were created using the software Vesta [5]

Recent work on MTa_2O_6 looked at the magnetic properties of single crystals along specific crystallographic directions, keeping in mind the role played by anisotropy [6].

Interesting magnetic properties were found in $NiTa_2O_6$, $CuSb_2O_6$ and $CoSb_2O_6$ [7] [8] [6]. The magnetism of trirutiles were explained based on the presence of two antiferromagnetic sublattices oriented at 90 degrees to each other [6]. This had the direct consequence that the application of external magnetic field produced two transitions instead of one. The compound was also seen to display moderate magnetocaloric effect. Interestingly, competing effects arising from antiferromagnetic (Neel), spin liquid and dimers were proposed in $CoSb_2O_6$ [6].

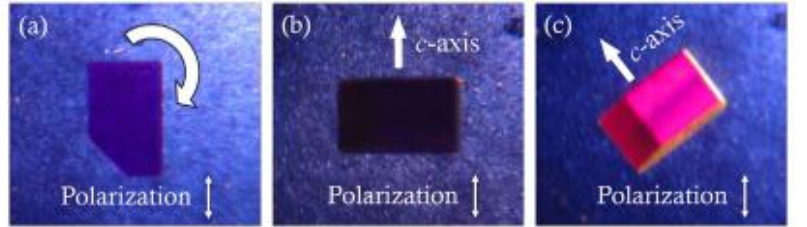
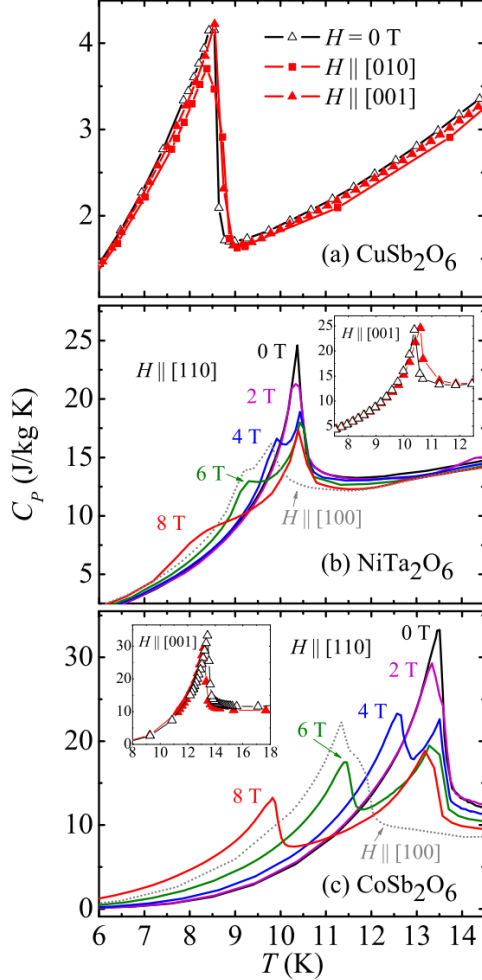


Figure 1.2: (Left) The specific heat of $CuSb_2O_6$, $NiTa_2O_6$ and $CoSb_2O_6$ were seen to display anisotropic effects in the presence of external magnetic field [6]. (Right) A single crystal of $CoTa_2O_6$ was demonstrated as displaying optical dichroism [9].

The magnetism of Ta-based trirutile single crystals were studied recently [9]. This study confirmed the $T_N = 6.12$ K for $CoTa_2O_6$. Anisotropy effects in magnetic susceptibility were clearly visible. Once again, the anisotropic effect of magnetic field on magnetic phase transitions and the consequent magnetocaloric effect was documented in this work.

The observation of sublattice effects and magnetocaloric effect implied a strong coupling between the spins and the lattice in this class of materials. This was indeed the case as observed

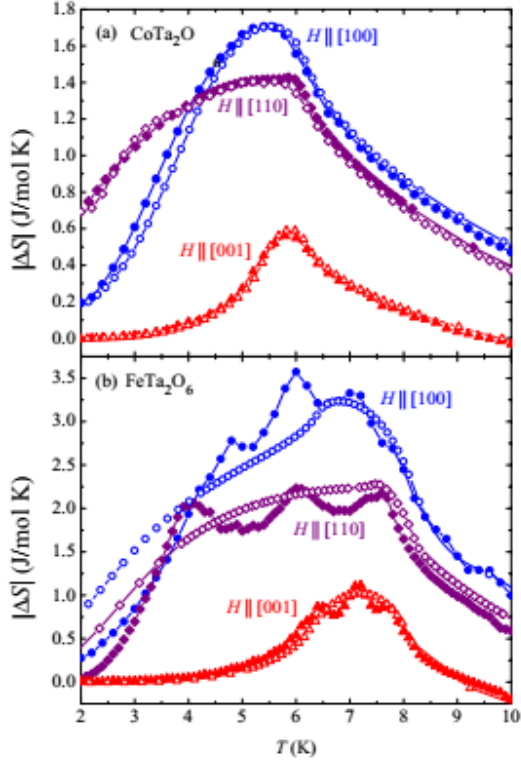


Figure 1.3: The magnetocaloric effect observed in CoTa_2O_6 and FeTa_2O_6 . Note that this is an anisotropic effect observed due to magnetic field being applied along different crystallographic directions [6].

The CoTa_2O_6 - FeTa_2O_6 phase diagram of mixtures were investigated using X-ray and neutron scattering and magnetization studies to identify a bicritical region in the x - T phase diagram (here, x is the concentration of Co in the formula $\text{Fe}_{1-x}\text{Co}_x\text{Ta}_2\text{O}_6$) [11]. For the Co-rich part of the phase diagram, all the compositions showed a magnetic structure with the propagation vector $(\pm \frac{1}{4} \frac{1}{4} \frac{1}{4})$. The bicritical region in the x - T phase diagram occurs at $x = 0.46$ and $T = 4.9$ K. The origin for the bicritical phase diagram was attributed to the competing magnetic and crystallographic structures. Another neutron diffraction report states that the magnetic moments of CoTa_2O_6 entirely lie on the Co-planes having propagation vector $(\pm \frac{1}{4} \frac{1}{4} \frac{1}{4})$ which leads to two-

in experimental investigations involving the study of thermal expansion [10]. Significant suppression of the thermal conductivity was observed along all the crystallographic directions in the case of Ta-based compounds as opposed to the Sb-based compounds. The experimental thermal conductivity data was explained based on resonant scattering of phonons in a two-level system with an energy splitting of the order of 100-150 K. This was attributed to the presence of a lower optic phonon mode in the Ta-based trirutiles.

dimensional magnetic structure [2]. Despite these efforts to study the magnetic structure of CoTa_2O_6 to understand the low dimensional magnetism, anisotropic exchange interactions that respond differently in external magnetic field and the magnetocaloric effect, the results presented in the aforementioned papers do not seem trustworthy or complete. In the work by Kiasat *et al* [2], the sample of CoTa_2O_6 contained CoO and Ta_2O_6 as impurities, thereby rendering the magnetic structure estimation questionable. Their previous work [11] on the bicriticality is on a mixed composition or used a sample from the same batch. Hence, we understand that the question of correct magnetic structure of CoTa_2O_6 is not yet fully addressed. At the same time, we want to understand the magnetic properties of low dimensional Co-chains in this compound consequent to dilution with a non-magnetic entity to realize spin dimers of Co. With this motivation, we prepared a series of trirutile compounds $\text{Co}_{1-x}\text{Mg}_x\text{Ta}_2\text{O}_6$ ($x = 0, 0.1, 0.3, 0.5, 0.7$, and 1). It has been reported [10] [12] [13] that many trirutile shows short-range magnetic order with reduced dimensionality of spins bounded by weak magnetic interactions. So, we want to investigate whether the Co moments would form dimers or clusters and further, to investigate the nature of spin correlations. This study would then form the preliminary basis for the future work to examine the magnetic excitations resulting from the ground state. Interestingly, the magnetic excitations or the magnons originating from trirutiles or their spin-phonon coupling has not been studied so far using neutron scattering techniques. It is the aim of the present work to form the framework for such a future work.

In the present thesis, to study structural, magnetic and thermodynamic properties in the series of compounds ($\text{Co}_{1-x}\text{Mg}_x\text{Ta}_2\text{O}_6$, where, $x = 0, 0.1, 0.3, 0.5, 0.7$, and 1) powder X-ray diffraction, magnetization, specific heat and neutron powder diffraction techniques were employed. All the samples were prepared using standard solid-state reaction method. Powder X-

ray diffraction patterns were measured in Rigaku min-flex 660I. The magnetization for the series of compounds was carried out in a Physical Property Measurement system (PPMS), Quantum Design using the susceptibility option. The specific heat of the series of compounds were measured using the specific heat option in the PPMS. To obtain qualitative and quantitative information about nuclear and magnetic structures, neutron diffraction data were gathered both at room temperature and at low temperature using a high-resolution neutron powder diffraction at University of Missouri Research Reactor (MURR).

Chapter 2: Theoretical Background

2.1 CRYSTAL STRUCTURE

A crystal structure forms when group of atoms called basis, is attached to every lattice point. A regular arrangement of points in the space are called lattice points. Precisely, we can say that when the basis of atoms is uniformly attached to every lattice point, crystal structure forms [14].

There are all together seven different type of crystal systems: (1) cubic, (2) tetragonal, (3) orthorhombic, (4) monoclinic, (6) triclinic, (7) trigonal and (8) hexagonal. Among them we are focus only on the tetragonal crystal system in the present thesis. This tetragonal crystal system has $a = b \neq c$ and $\alpha = \beta = \gamma = 90^\circ$. Here, a , b and c are the lattice constants, and α, β , and γ are the angles between b and c , a and c and a and b respectively. [15]

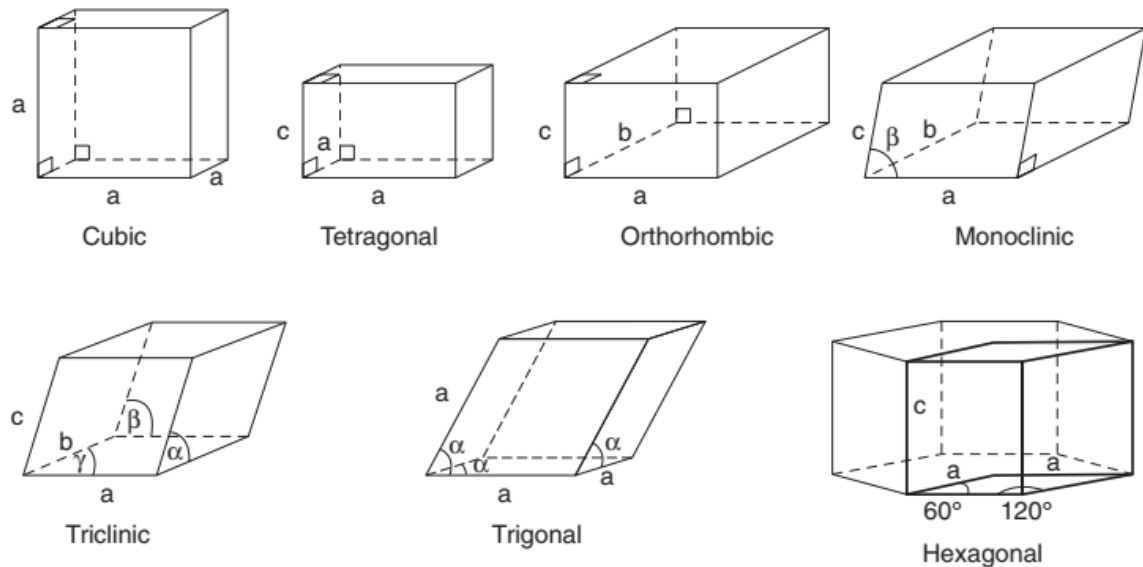


Figure 2.1: Seven different type of unit cell [15]

2.2 POWDER X-RAY DIFFRACTION (PXRD)

X-ray diffraction is a basic tool for crystal structure analysis and phase identification of the crystalline materials. The powder X-ray diffraction technique that we use extensively in this thesis is for phase identification and study of crystal structure is based on the Bragg's law, is shown in figure 2.2. The X-rays that are reflected specularly from the parallel planes of atoms in the crystal, are superimposed to give the diffraction pattern. These diffraction patterns are result of constructive interference of the scattered X-ray beams. As a first approximation, it is assumed that the scattering is completely elastic and there is no loss of energy of incident X-ray after reflection from the atoms. Scattered X-ray beams interfere constructively if the path difference of diffracted beam is equal to an integral multiple of wavelength of incident X-rays.

Mathematically, we can write the Bragg's law as,

$$2d \sin \theta = n\lambda \quad (2.1)$$

Where d represents interplanar distance, θ is the glancing angle, n is the integer number showing the order of reflection and λ is the wavelength of the monochromatic incident X-rays. Bragg's reflection occurs only if the wavelength of the incident X-ray wave is comparable to the size of the scattering object (i.e. $\lambda \leq 2d$).

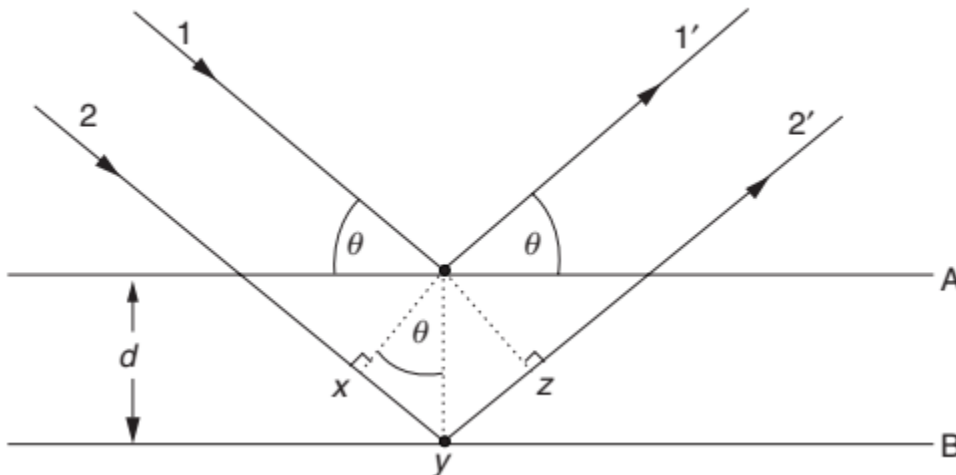


Figure 2.2: Represents the geometrical figure of Bragg's law [15].

In the above figure; 1, 2 represent incident monochromatic X-rays and 1', 2' represent respective reflected rays. A & B are the consecutive atomic planes and the dark circles represent two nearest atoms of consecutive planes and d is the distance between two consecutive atomic planes (A and B). Also $xy = yz = d \sin \theta$

2.2.1 PXRD instrument

For the characterization of powder samples for its phase purity and crystal structure, the Rigaku Miniflex 600I diffractometer was used. It is also called benchtop diffractometer. The instrument has 600 W fixed x-ray tube and a fixed detector; however, it has rotating sample stage. It has copper target which produces the x-ray of wavelength 1.485 \AA . The tube produces the divergent x-ray beam which is collected by silicon strip detector after reflection from the sample.

2.3 ELASTIC NEUTRON DIFFRACTION

Elastic (where there is no energy transfer involved) powder neutron diffraction is like X-ray diffraction, but it can provide information about magnetic structure in addition to nuclear structure of the material. In an elastic neutron diffraction experiment, the powder sample is placed on the path of neutron beam and the scattered neutrons from the sample are recorded by the detector. The diffraction pattern thus obtained can provide the structural information of the sample. Neutron being chargeless, they have high penetrating power so they can penetrate the surface of the material and can provide information on the interior structure of material. Furthermore, neutron has magnetic moment so they can be used to study the magnetic structure of the material or sample [16].

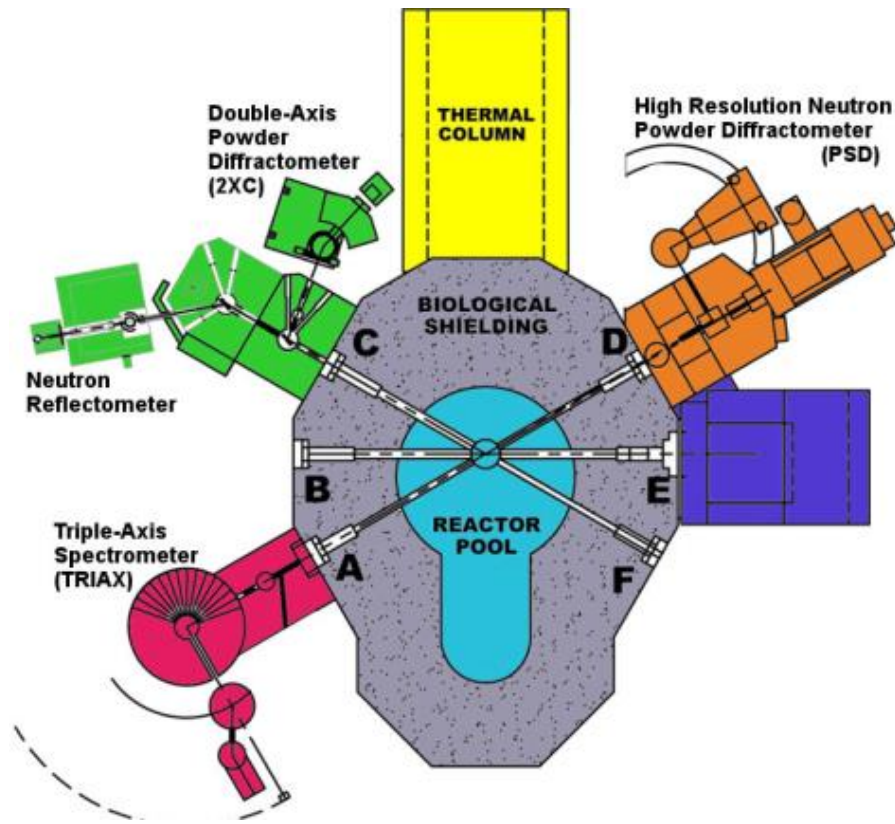


Figure 2.3: This is the architecture diagram of the reactor and instrumental beamline in MURR (Missouri University Research Reactor).

The architecture diagram of nuclear reactor in MURR is shown in above Figure 2.3. There is a pool at the center of the reactor, shown in blue color. High Resolution Neutron Powder Diffractometer PSD is shown in right top side of the pool in brown color. Similarly, at left top side Double-Axis Powder Diffraction (2 XC) and Neutron Reflectometer are situated which are shown in green color. The Triple-Axis Spectrometer (TRIAx) shown in left bottom side of the pool. Similarly, biological shielding and thermal neutron chamber are shown in dark gray and yellow colors, respectively. We used PSD instrument for the measurement of elastic neutron diffraction.

Neutrons coming out from the nuclear reactor have very high speed about 14000 km/s and has energy about 1 MeV. These fast-moving neutrons are slow down by passing through cold sources and these cold sources are simply the container containing hydrogen or deuterium at cold temperature. For elastic scattering of the powder sample, we use neutrons having energy around 0.0373 eV, and the energy lies in the range of thermal neutrons [16]. The wavelength of thermal neutrons is given by,

$$\lambda = \frac{h}{mv} \quad (2.2)$$

where $h = 6.62 \times 10^{-34}$ Js the Planck's constant, m and v are mass and velocity of neutron respectively.

Equivalently, the above equation (2.2) can be written as,

$$\lambda = \frac{h}{\sqrt{2mk_B T}} \quad (2.3)$$

Where k_B is the Boltzmann constant and T is the temperature.

For room temperature, $T = 300$ K, wavelength of neutron $\lambda \approx 2 \text{ \AA}$. i.e wavelength of neutron is comparable to the atomic distance. So thermal neutrons are suitable for the study of atomic and magnetic structure of any sample or material. [17]

For our samples we used the High-Resolution Neutron Powder Diffractometer (PSD) at University of Missouri Research Reactor (MURR). Thermal neutrons having wavelength 1.485 \AA were employed. The instrument covers the angular range from $5^\circ - 105^\circ$ varying temperature from 5 K to 800 K. The neutron beam can be focused in both vertical and horizontal direction. The 9 Frankuchen cut Si (511) blades are used to focus beam in vertical direction and by applying bending strain, horizontal neutron beam can be focused.

Table I: Energy and wavelength of cold, thermal and hot neutrons [18]

Types of neutrons	Energy (meV)	Wavelength (Å)
Cold neutron	0.1-5	4-30
Thermal neutron	5-100	1-4
Hot neutron	10^8 - 10^{10}	$9 \times 10^{-4} - 9 \times 10^{-5}$

2.3.1 Neutron scattering cross-section

X-rays are diffracted by the electronic distribution of atoms; however atomic nuclei are responsible for the scattering of the neutrons. Also, in case of magnetic samples i.e. magnetic nuclear scattering, neutrons get scattered if their magnetic moment interact with magnetic moment of atoms. Such scattering takes place only if the size of the scattering object is comparable to the wavelength of neutrons.

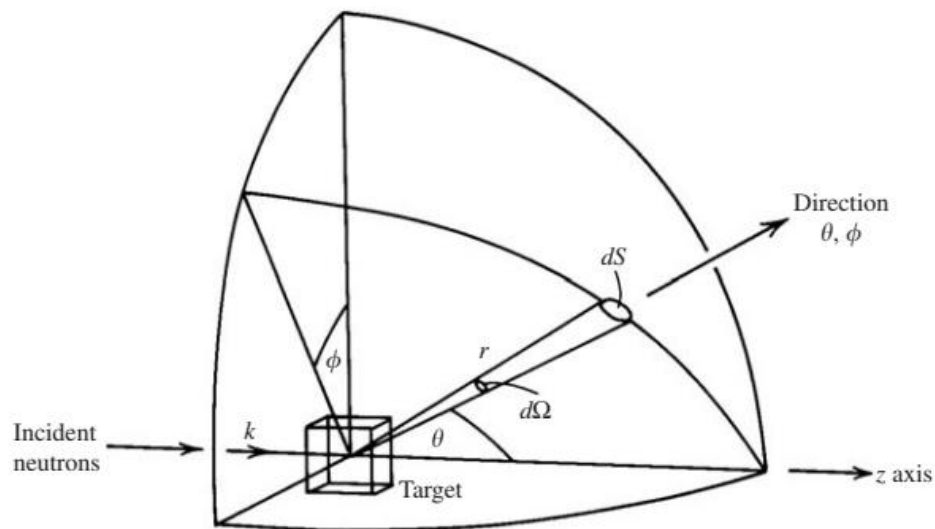


Figure 2.4: Geometrical figure of neutron scattering cross-section. (Marshall and Lovesey 1971; Squires 1978)

2.3.2 Scattering cross-section

The neutron scattering cross-section refers to the ability of the target atoms to scatter the incident neutrons. It can be defined as the ratio of the neutrons scattered by the target atoms per second to the number of neutrons incident per unit area per second (i.e. incident neutrons flux).

$$\text{Scattering cross-section}(\sigma) = \frac{\text{number of neutrons scattered per second}}{\text{incident neutron flux}}$$

The typical values of scattering cross-section for Co, Ta and O are 5.6(3), 6.01(12), and 4.232(6) respectively. [19]

For an incident neutron flux of wave vector $k(=\frac{2\pi}{\lambda})$, the scattered neutron flux detected by the detector of angular element $d\Omega(=\sin\theta d\theta d\phi)$ is given by $\left(\frac{d\sigma}{d\Omega}\right)d\Omega$. Where $\frac{d\sigma}{d\Omega}$ is the differential scattering cross section and (θ, ϕ) are the polar coordinates of the position of the detector. We have assumed that the scattering is completely elastic and nucleus is rigid and fixed. If the neutrons falling on the sample have plane wave function i.e. $\Psi_i = e^{ikz}$, then, the beam of neutrons which are scattered from the sample/target will have spherical symmetry and can be represented as $\Psi_s = \frac{-b}{r} e^{ikr}$. Here, k is the wave vector and is equal to $2\pi/\lambda$; r represents the distance between the detector and the scattering atom and b is the nuclear scattering length and is a complex number. Thus, the scattering cross section can be written as,

$$\begin{aligned} \sigma &= \frac{\text{flux of scattered neutrons in the direction of } (\theta, \phi)}{\text{flux of incident neutrons}} \\ \sigma &= \frac{4\pi r^2 v \left| \left(-\frac{b}{r}\right) e^{ikr} \right|^2}{2} \\ \sigma &= 4\pi b^2 \end{aligned} \tag{2.5}$$

Here, v is the neutron velocity and the imaginary part of the scattering length b is responsible for the absorption of neutron. However, most of the compounds and elements have low value of

absorption and b can be consider as the real constant. [17] The typical value of scattering length and absorption coefficient for Cobalt are 2.49(2) and 37.18(6). [19]

2.3.2 Coherent and incoherent neutron scattering

X-ray scattering is always coherent, as only electrons are responsible for the scattering and all the electrons distributed around the atoms have identical power of scattering. However, neutron scattering completely depends on σ and b of the scattering material. If the scattering sample is composed of the atoms of same species, the neutrons are scattered in the same way and this type of scattering is called coherent scattering. If the scattering sample is composed dissimilar atoms, they have a mixture of scattering centers. Such mixtures of scattering centers can lead to randomness in the scattered neutrons because all the atoms cannot respond to the neutrons in an identical way. We may lose the similarity in the scattering pattern and this leads to the incoherent neutron diffraction [16].

The total differential cross section can be written as the sum of coherent and incoherent differential cross section;

$$\frac{d\sigma}{d\Omega} = \left(\frac{d\sigma}{d\Omega}\right)_{coherent} + \left(\frac{d\sigma}{d\Omega}\right)_{incoherent} \quad (2.6)$$

$$\text{Total cross - section} = \int \frac{d\sigma}{d\Omega} ds \quad (2.7)$$

2.3.3 Magnetic scattering

Magnetic scattering of neutron arises due to its magnetic moment, which interact with the orbital and spin magnetic moments of the atoms in a solid. In case of single atom, the magnetic scattering is due to unpaired electron spins. Scattering will occur when the electronic distribution is comparable to the size of thermal neutrons, and the interference phenomena thus occurs

further leads to the magnetic form factor. The differential magnetic neutron scattering cross-section per unit atom is given by,

$$\left(\frac{d\sigma}{d\Omega} \right)_{mag} = q^2 S^2 \left(\frac{e^2 \gamma}{mc^2} \right) f^2 \quad (2.8)$$

Here, q is the magnetic interaction vector, S is spin quantum number of target atom, e and m are the charge and mass of the electron. Similarly, c represents speed of the light, γ is the magnetic moment of the neutron and f represent magnetic form factor. From the quantum number S the scattering cross-section depends on the valance state of ion or atom and for the contribution of orbital moments, $2S$ is replaced by gJ .

Here, g is called lande splitting factor and is written as,

$$g = 1 + \frac{J(J + 1) + S(S + 1) - L(L + 1)}{2J(J + 1)} \quad (2.9)$$

The degree of correlation of magnetic moment of the assembly of atoms varies from zero to unity (i.e. for paramagnetic ≈ 0 and ferromagnet ≈ 1). In case of completely disordered paramagnetic system, we can observe the incoherent scattering as the average of q over all the orientation is $\frac{\pi}{4}$. This leads to the destructive interference phenomena; however, it still contributes for the background of powder diffraction pattern.

Thus, we can write the total cross-section as;

$$\sigma_{total} = \sigma_{coh} + \sigma_{incoh} + \sigma_{NM} + \sigma_M + \sigma_{pol} \quad (2.10)$$

Where, σ_{coh} and σ_{incoh} are the coherent and incoherent nuclear scattering cross sections; σ_{NM} and σ_M are nuclear magnetic and magnetic scattering cross section terms, and σ_{pol} is polarization term. So, if we take a simple magnetic structure having co-linear moments (i.e. neglecting

incoherent scattering terms), the differential cross-section becomes,

$$\frac{d\sigma}{d\Omega} = b^2 + 2bp\hat{\mathbf{P}} \cdot \mathbf{q} + p^2 q^2 \quad (2.11)$$

Where, $\hat{\mathbf{P}}$ represents the unit vector of polarization of incident thermal neutrons. For simple structure, $\sigma_{pol} = 0$, and the remaining terms are nuclear, magnetic and nuclear-magnetic interaction. For unpolarized incident neutrons, the interaction terms in average reduces to zero and the above equation (2.10) becomes,

$$\frac{d\sigma}{d\Omega} = b^2 + p^2 q^2 \quad (2.12)$$

2.3.4 Diffracted neutrons from ideal polycrystalline material

For the diffraction of the neutrons from the sample, we assume that the crystal is composed of perfectly parallel flat planes having uniform scattering density and the scattering density is concentrated only on the nucleus of the atom.

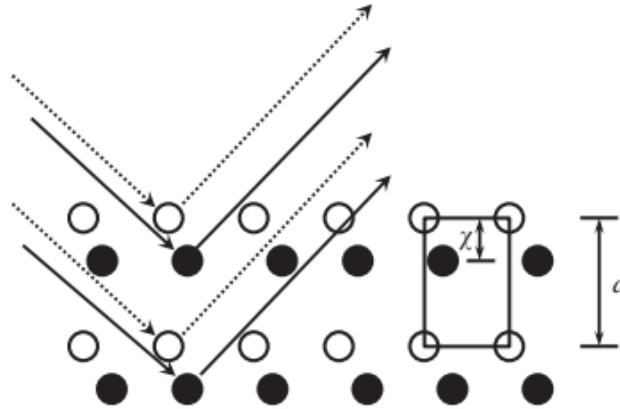


Figure 2.5: 2D figure of diffraction of neutrons from parallel planes [17].

The maximum or minimum intensity of scattered neutron wave depends on the phase difference of two scattered waves from the target atoms. The maximum intensity is observed if the phase difference between two light or two dark atoms is 2π or 0. But if the phase difference

between two adjacent light and dark atoms is $2\pi h\chi$ ($\chi = \frac{x}{a}$), where χ is the distance between two adjacent atoms (dark circle and full circle atoms) and x is the path difference. The scattered waves can cancel more or less with the reduced intensity.

In 3D, the phase difference between a dark and a bright atom at the origin is given by,

$$\phi = 2\pi(hx + ky + lz) \quad (2.13)$$

Here, h, k, l are the Miller indices of the reflecting plane and (x, y, z) are the fractional coordinates of the atom which is inside the unit cell having dimensions a, b , and c .

The equation of the scattered wave from any atom can be written as,

$$A e^{i\phi} = b e^{2\pi i(hx + ky + lz)} \quad (2.14)$$

Where, A represents the amplitude of the scattered wave.

And the structure factor can be expressed as,

$$F_{hkl} = \sum_n b_n e^{2\pi i(hx_n + ky_n + lz_n)}$$

$$F_{hkl} = \sum_n b_n e^{2\pi i(\mathbf{H}_{hkl} \cdot \mathbf{r}_n)} \quad (2.15)$$

Where, \mathbf{r}_n is the position vector of n^{th} atom and equation (2.14) and (2.15) represents Fourier transform of the charge density at reciprocal lattice points. [17]

2.4 RIETVELD ANALYSIS

Rietveld analysis technique was initially projected by Hugo M. Rietveld to analyze neutron pattern. Later, it was extensively used for refining the x-ray and neutron powder pattern, as it can perform whole pattern fitting instead of single peak analysis. These days Rietveld analysis is a basic tool to probe structural and magnetic information of the given powder samples. Structural information refers to the lattice parameters, atomic positions, occupancy, etc.

However, a high-quality experimental diffraction pattern is required for profile fitting and modeling the data model, to examine powder diffraction pattern.

The basic principle of profile refinement is based on the least square refinement, which is demonstrated by the function which has to be minimized with respect to the parameters. The function which has to be minimized in the Rietveld method is;

$$\chi^2 = \sum_i w_i (y_{obs} - y_{cal})^2 \quad (2.16)$$

Where, $w_i = \frac{1}{\sigma_i^2}$ and σ_i^2 is a variance of the observed data. Similarly, y_{obs} and y_{cal} are the observed and calculated intensities at each step. The summation represents the sum of all points in the diffraction pattern. It requires many the least square approach for the refinement continues until the theoretical profile line matches the measured profile [20].

Peak positions, intensities and shapes are other important powder diffraction profiles. Peak positions in the diffraction pattern are determined by Bragg's law using wavelength and d-spacing of unit cell. However, the peak intensities depend on the lattice parameters and the atomic coordinates. Peak shapes of the powder pattern is influenced by various factors via, sample size and shape, characteristic of incident beam and the instrument used for diffraction. For instance, if we use monochromatic neutron beam, the peaks obtained in the diffraction pattern are Gaussian shape. The width of the peaks extends out with the increase of Bragg angles. And the angular dependency can be represented by the following equation,

$$H^2 = w + v \tan\theta + u (\tan\theta)^2 \quad (2.17)$$

It is also called the Caglioti formula. H represents full widths at half maximum (FWHM), and u , v and w are halfwidth parameters which are refined during the Rietveld analysis. Beside halfwidth parameters, lattice parameters, background, atomic positions and in some case occupancy number must be refined one by one until we get a good profile fitting. The best way to know whether the refinement we did is fruitful or not is given by difference between observed

and calculated data. The difference has to be flat in order to get the best fit [20]. Beside this R -values provide the quality of fit. They are listed below:

a) Profile factor;

$$R_p = 100 \frac{\sum_i |y_{Obs} - y_{Cal}|}{\sum_i y_{Obs}} \quad (2.18)$$

b) Weighted profile factor;

$$R_{wp} = 100 \left[\frac{\sum_i |y_{Obs} - y_{Cal}|^2}{\sum_i w_i y_{Obs}^2} \right]^{\frac{1}{2}} \quad (2.19)$$

c) Expected weighted factor;

$$R_{exp} = \left[\frac{n - p}{\sum_i w_i y_{Obs}^2} \right]^{\frac{1}{2}} \quad (2.20)$$

Where, n represents the total number of points used in the refinement, which is the difference of total number of points in the pattern and total number of excluded points. And, p is the number of refined parameters.

d) Indicator for goodness of fit;

$$S = \frac{R_{wp}}{R_{exp}} \quad (2.21)$$

e) Reduced chi-square;

$$\chi^2 = \left[\frac{R_{wp}}{R_{exp}} \right]^2 = S^2 \quad (2.22)$$

f) Bragg Factor;

$$R_B = 100 \frac{\sum_j |I_{Obs} - I_{Cal}|}{\sum_j |I_{Obs}|} \quad (2.23)$$

Where, I_{Obs} and I_{Cal} are observed and calculated integrated Bragg intensities without background. All these R -values are significant if only if they are calculated from background removed intensities [20]. A good fit has low R -values and $1 < \chi^2 < 5$.

The software like Fullprof, GSAS, Rietica etc can be used for the Rietveld refinement. We employed Fullprof for the analysis of neutron and x-ray powder diffraction pattern for analysis of PXRD and neutron diffraction pattern. And the best way to start to refine is to copy PCR file (input control file) and modify it according to the need of the refinement; x-ray,

neutron, and magnetic structure. It is always necessary to collection the information about profile shape function, lattice and instrumental parameters and the experimental conditions before running any Rietveld refinement.

2.5 MAGNETIC PROPERTIES

Magnetic moment of a material measures the strength and direction of its magnetism. The term magnetism refers to the magnetic dipole moment. Any magnetic substance like a bar magnet or a current in a loop, has magnetic moment. An electron moving around the atom also has magnetic dipole moment due to its spin. The alignment of these magnetic moment in any material gives rise to magnetism. Depending on the alignment of magnetic moments with or without external field, we can classify Ferromagnetism, Antiferromagnetic, Ferrimagnetism, Para magnetism, and Diamagnetism.

2.5.1 Magnetic interaction

Magnetic interactions take place between two ions through the direct overlap of the wave functions, and the coupling of magnetic moments between ions or atoms give rise to magnetism in many materials. The quantum mechanical interaction which arises due to the change in the expectation value of energy of two identical particles through the overlap of wave functions is called exchange interaction. The exchange interaction between neighboring magnetic ions are responsible for individual moments to align parallel or antiparallel alignment with their neighboring atoms or ions. Generally, there are four types of exchanges, viz Direct, Indirect, Double and Anisotropy. The exchange which operates between the moments which lie very close to each other i.e. they are sufficiently close to overlap their wave functions is called Direct exchange. They are short range and has very strong coupling. Similarly, if the interaction between ions are mediated through an intermediary, like electrons, the exchange is called

Indirect exchange. Such exchange takes place on the metals where there is no direct overlapping between neighboring magnetic orbitals, i.e. its long-range coupling. Similarly, if the interaction between the ions is mediated by the non-magnetic ions, then we call it as Superexchange. Double exchange can be observed in the oxides in which the magnetic ion has mixed valency, so that it can have more than one oxidation state. And such exchange mechanism is seen in ferromagnetic alignment. Finally, the exchange interaction occurring between excited state of one ion and ground state of the other ion is called the Anisotropic exchange. [21]

The magnetic interactions that operate between the magnetic moments in a solid give rises to different types of ground states, which includes, antiferromagnets, ferromagnets, and spin glasses.

2.5.2 Antiferromagnetism and ferromagnetism

An ideal antiferromagnet has zero net magnetic moments with their spins in the direction opposite to each other. In order to interpret antiferromagnetism, we can consider the system as composed of two sublattices having equal magnetizations, but oriented in opposite directions. They have negative exchange interaction as a result of the nearest neighbor magnetic moments being antiparallel to one another. However, in ferromagnets, the magnetic moments are directed in the same direction and positive dominant exchange interaction is responsible for such effect. Ferromagnets have magnetic moments even in null magnetic fields i.e. they have strong spontaneous magnetization. [21]

2.5.3 Magnetic susceptibility

Magnetic susceptibility is given by the ratio of magnetization to the magnetic field intensity.

$$\chi = \frac{M}{B} \quad (\text{C. G. S}) \quad (2.24)$$

It is a unitless physical quantity and a basic parameter to probe magnetic properties. For ferromagnetic substance $\chi < 1$, however, for antiferromagnetic, χ is positive and almost equal to paramagnetic materials.

2.5.4 Curie-Weiss law

For simple paramagnetic substance, there is an inverse relation between temperature and susceptibility (χ), this is called Curie law of magnetism.

$$\chi = \frac{C}{T} \quad (2.25)$$

Here, C represent the curie constant and is given by $C = Ng^2\mu_B^2 \frac{S(S+1)}{3k_B}$. Here, N is the Avogadro's number, g is the Landé g-factor, μ_B is the Bohr magneton S is the spin value and k_B is the Boltzmann constant. The magnetic susceptibility with Curie Weiss dependence is given by,

$$\chi \propto \frac{1}{T - \theta} \quad (2.26)$$

This is also called Curie-Weiss law. Here, θ is the Weiss temperature. If $\theta < 0$, $\theta > 0$ and $\theta = 0$ represents antiferromagnetic, ferromagnetic and paramagnetic material respectively. As we lower the temperature for antiferromagnetic materials, χ is reduced, which reflects that magnetic structures are ordered. But the rise in temperature can thermally induced disorder and increases the value of χ i.e. χ has maximum value at T_N and decreases at higher temperature following Curie-Weiss law. [15]

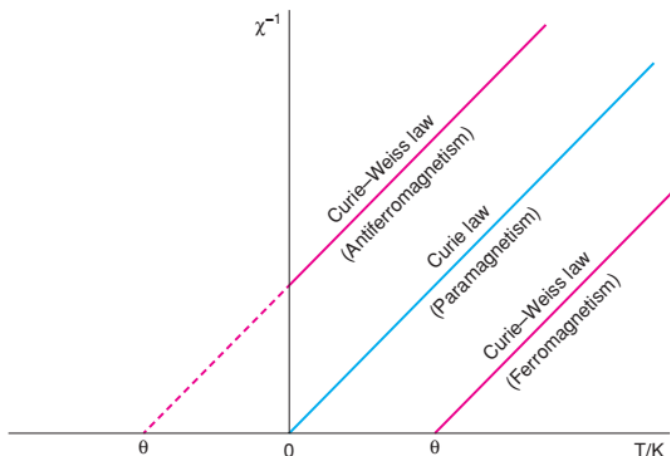


Figure 2.6: Plot between $1/\chi$ and Temperature (K) for various substance [15]

2.5.5 Spin chains

A linear chain of spins in one dimension makes a spin chain. Generally, two types of spin chains exist, either Ising or Heisenberg. In Ising spin chains, individual spins are forced to point either parallel or antiparallel in a particular direction, on the other hand, Heisenberg spins can freely point in any direction. Such type of spin chains is observed on the compounds having general formula ABX_3 . Here, A & B are non-magnetic and magnetic cations, having single and doubly charged respectively. X is halide anion. For instance, CsCoCl_3 shows the 1-D Ising spin chain whereas, KCuF_3 shows 1-D Heisenberg spin chain. Such system most of the time can lead to 3-D long range magnetic order which may be due to small interchain interaction which can link the chain together.

2.5.6 Two-dimensional magnetism

In the present thesis, we are concerned about A_2BX_4 type compounds that display low dimensional magnetism. Here, A is a singly charge non-magnetic cation, B is a magnetic cation with doubly charge and X is a halide. These compounds adopt tetragonal structure where magnetic ions sit on each corner of square lattice in 2-D. One and two-dimensional bulk

magnets, do not show long range magnetic order at finite temperature due to the thermal fluctuations. Even at $T = 0$, long range order is not observed for spin-1/2 Heisenberg antiferromagnets in one-dimension. When the temperature of two-dimensional (square lattice) Heisenberg antiferromagnet is reduced, the short-range ordering of correlated regions grows. And the size of such ordering is simply called a correlation length or spin-spin correlation length. Correlation length shows diverge exponentially behavior for lower temperature and leads to long range magnetic ordering at $T = 0$. [21]

2.6 SPECIFIC HEAT CAPACITY OF A CRYSTALLINE SOLID

Generally, specific heat refers to the heat capacity of a crystalline solid at constant volume, C_V . Classically, heat capacity of the solid is given by $3NR$, where N represents no of atoms in the solid and R represents molar gas constant. Classical theory of specific heat is well satisfied at higher temperature for most of the element. However, for heavy and light elements like Boron, Carbon and Silicon there was high disagreement between experimental values and theoretical values as predicted by classical theory. Also, as the temperature falls below certain value the classical law completely fails and $C_V \rightarrow 0$ at $T=0$. Thus, classical approach of heat capacity cannot well explain the variation of heat capacity with all range of temperature. So later, Einstein proposed a theory of specific heat based on quantum theory [14].

2.6.1 Einstein theory of specific heat of a solid

Einstein assumed that all the atoms of the solid vibrate simple harmonically about their mean position with same frequency and used Plank's distribution law to calculate the mean energy. The mean energy of solid per degree of freedom is $\frac{h\nu}{e^{h\nu/kT}-1}$

And, the specific heat capacity of solid calculated by Einstein is [14]

$$C_V = (\partial U / \partial T)_V$$

$$C_V = 3Nk \left(\frac{h\nu}{kT} \right)^2 \frac{e^{h\nu/kT}}{(e^{h\nu/kT} - 1)^2} \quad (2.27)$$

2.6.2 Debye theory of specific heat of a solid

Einstein theory of specific heat capacity was able to address the specific heat capacity of solid at room temperature and higher temperature. But there was some disagreement between experimental and theoretical values at low temperature. To correct this discrepancy, Debye proposed the theory of heat capacity and assumed that atoms in the crystal are not isolated oscillators vibrating at the same frequency but as a system of couple oscillators having $3N$ normal modes of vibrations and each has its own natural vibrating frequency. i.e. the system is composed of $3N$ independent harmonic oscillators. For low frequency vibrations, (if the wavelength is $\lambda \gg a$, atomic lattice) crystals are treated as the homogeneous elastic medium.

The specific heat capacity of solid as calculated by Debye is given by

$$C_V = 9Nk \left(\frac{1}{x_D^3} \int_0^{x_D} \frac{x^4 e^x dx}{(e^x - 1)^2} \right) \quad (2.28)$$

Where, $x = \frac{h\nu}{kT}$, $x_D = \frac{h\nu_D}{kT} = \frac{\theta_D}{T}$ and θ_D is called a Debye temperature.

For higher temperature above equation reduces to $3Nk$. But for lower temperature it reduces to

$$C_V = \frac{12}{5} \pi^4 Nk \left(\frac{T}{\theta_D} \right)^3 \quad (2.29)$$

This is also called Debye's T^3 law. This agrees with experimental observations [22].

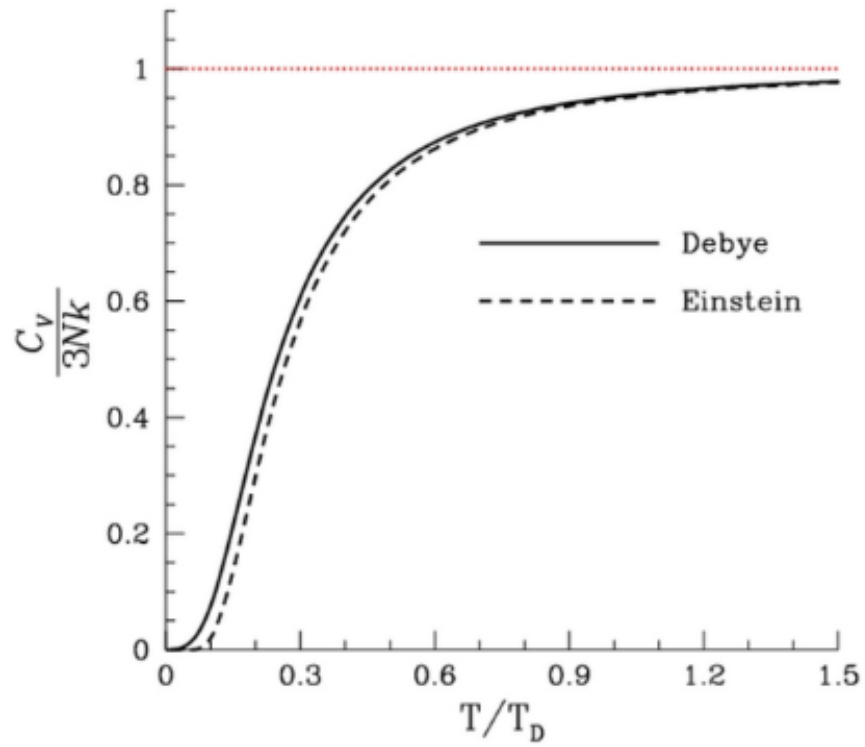


Figure 2.6: Normalized specific heat plotted as a function of normalized temperature (normalized with respect to Debye temperature, T_D) for both Einstein and Debye Models.
<https://en.wikipedia.org/w/index.php?title=File:DebyeVSEinstein.jpg>

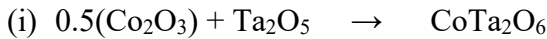
Chapter 3: Synthesis and Magnetic Properties of $\text{Co}_{1-x}\text{Mg}_x\text{Ta}_2\text{O}_6$

This chapter describes the details of the polycrystalline synthesis of the trirutile compounds, $\text{Co}_{1-x}\text{Mg}_x\text{Ta}_2\text{O}_6$, structural and phase characterization using X-ray diffraction and the magnetic properties of these compositions.

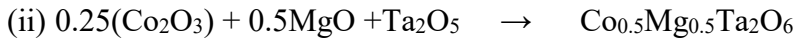
3.1 POLYCRYSTALLINE SYNTHESIS

Polycrystalline samples ($\text{Co}_{1-x}\text{Mg}_x\text{Ta}_2\text{O}_6$ for $x = 0.0, 0.1, 0.3, 0.5, 0.7$, and 1.0) were prepared by the conventional solid-state method [15] in which stoichiometric amount of precursor oxides, Co_2O_3 , MgO and Ta_2O_5 were used. All these oxides were of purity $\geq 4N$ which were purchased from Fisher Scientific. The stoichiometric amount of respective oxides were mixed and grinded in mortar and pestle. The ground powders were heated at 1350°C for 12 hours. The process of heating is repeated four times with intermediate grinding to make sure phase-pure samples of $\text{Co}_{1-x}\text{Mg}_x\text{Ta}_2\text{O}_6$ for $x = 0.0, 0.1, 0.3, 0.5, 0.7$, and 1.0 .

The balanced chemical reaction for CoTa_2O_6 and $\text{Co}_{0.5}\text{Mg}_{0.5}\text{Ta}_2\text{O}_6$ are shown below:



To prepare 1 gram of CoTa_2O_6 , we need $\text{Co}_2\text{O}_3 = 0.3209 \text{ g}$ and $\text{Ta}_2\text{O}_5 = 1.7100 \text{ g}$



Similarly, to prepare 1 g of $\text{Co}_{0.5}\text{Mg}_{0.5}\text{Ta}_2\text{O}_6$, we need $\text{Co}_2\text{O}_3 = 0.083 \text{ g}$, $\text{Ta}_2\text{O}_5 = 0.8847 \text{ g}$ and $\text{MgO} = 0.0403 \text{ g}$

3.2 CHARACTERIZATION OF POWDER X-RAY DIFFRACTION DATA

The powder X-ray pattern of the series of $\text{Co}_{1-x}\text{Mg}_x\text{Ta}_2\text{O}_6$ were collected in a Rigaku MiniFlex 600I diffractometer at room temperature with a Cu target employing the wavelength 1.548 \AA . The PXRD data were refined by using Full Prof Suite for the characterization of purity

of the samples and to elucidate the structural parameters. CoTa_2O_6 belongs to the space group $P4_2/mnm$. The PXRD pattern of the samples taken at $T = 300$ K are shown in the figure 3.1. We present the refined pattern for $x = 0, 0.3, 0.5, 0.7$ and 1. Note all the compounds show similar pattern which belongs to the trirutile structure. The black solid line in the figures are Rietveld fit

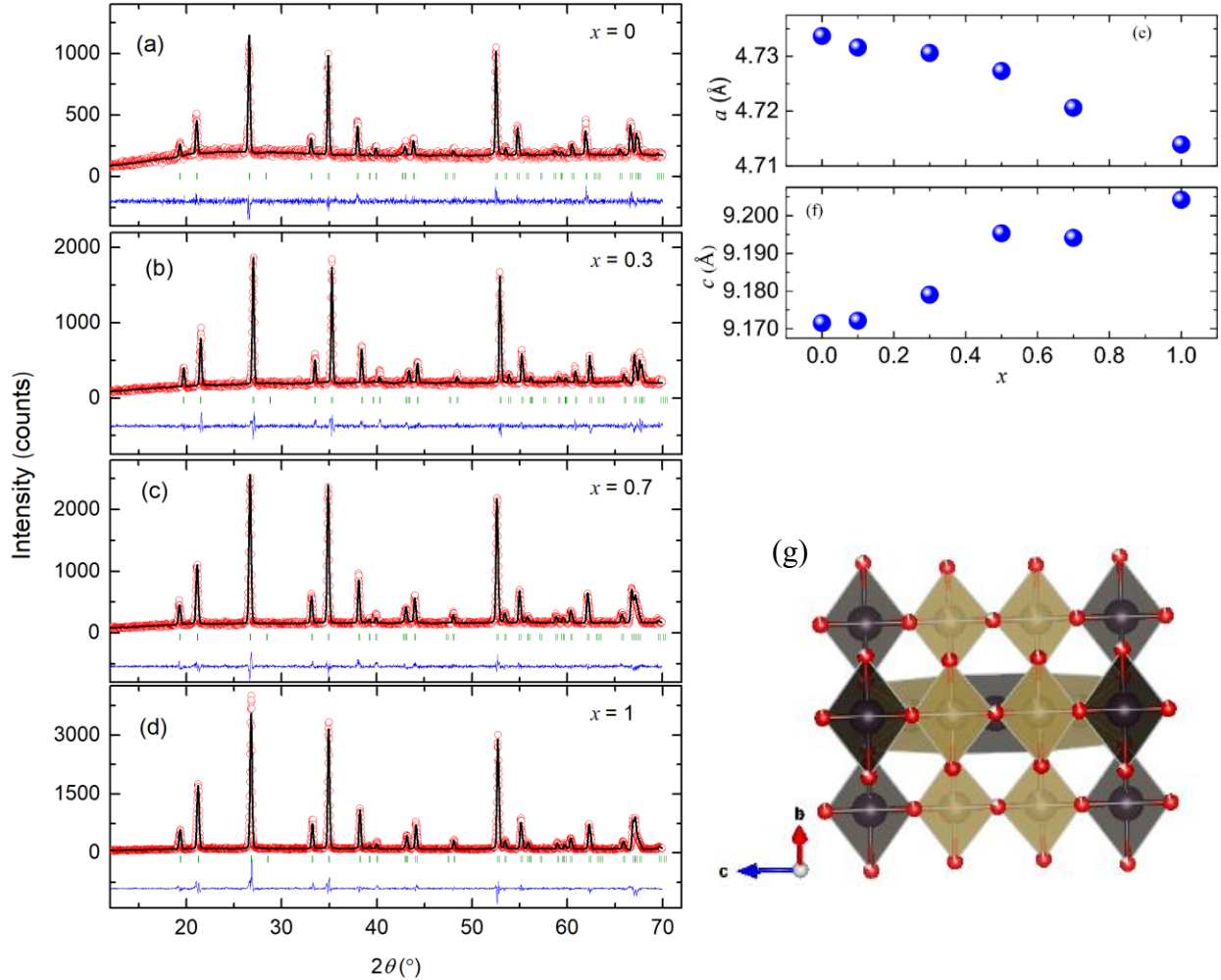


Figure 3.1: (a-d) The PXRD patterns for $\text{Co}_{1-x}\text{Mg}_x\text{Ta}_2\text{O}_6$ ($x = 0, 0.3, 0.7$ and 1) compositions. The structural analysis of these compositions done using $P4_2/mnm$ space group. The black solid line represents the fit, red circles represents the experimental PXRD data. The difference patterns are shown in blue and Bragg's peaks are shown by vertical tick marks. Figure 3.1 (e) and (f) represents the variation of lattice parameters with x . Figure (g) show the structural diagram of MgTa_2O_6 [5].

using the space group $P4_2/mnm$, which provided satisfactory fits. The black solid line in the figures are Rietveld fits using the space group $P4_2/mnm$, which provides satisfactory fits. The Figure 3.1(e & f) show the variation of lattice parameters a and c as the function of Mg-content(x). The lattice parameter $a = b$ decreases linearly as the Mg-content increases progressively. However, an exactly opposite trend is observed for lattice parameter c , which was expected as we doped Mg in place of Co lattice, because these two atoms have different atomic radii [13]. We also observed an anomaly for $x = 0.5$ while refining the lattice parameter c .

Table I below shows the refined lattice parameters of the different compositions of the $\text{Co}_{1-x}\text{Mg}_x\text{Ta}_2\text{O}_6$ series and the goodness-of-fit obtained as a result of the Rietveld refinement of PXRD patterns. The atomic parameters of CoTa_2O_6 were used as a straight point to perform refinements.

Table I: Lattice parameters, goodness of fit and volume of unit cell for $\text{Co}_{1-x}\text{Mg}_x\text{Ta}_2\text{O}_6$, $x = 0, 0.3, 0.7$ and 1 respectively. Fractional coordinates of atoms in the CoTa_2O_6 structure is shown.

	a (Å)	c (Å)	χ^2	$V(\text{Å}^3)$
CoTa_2O_6	4.7337(2)	9.1715(6)	1.18	205.51
$x = 0.1$	4.7316(2)	9.1721(4)	1.79	205.34
$x = 0.3$	4.7306(2)	9.1790(4)	1.49	205.41
$x = 0.5$	4.7273(1)	9.1953(3)	1.43	205.48
$x = 0.7$	4.7206(1)	9.1941(3)	1.4	204.88
MgTa_2O_6	4.7139(2)	9.2042(3)	2.33	204.52
Atom	Wyckoff pos.	x	y	z
Co	2a	0	0	0

Ta	4e	0	0	0.3309
O ₁	4f	0.3109	0.3109	0
O ₂	8j	0.2981	0.2981	0.3347

3.2 CHARACTERIZATION OF MAGNETIZATION DATA

To measure magnetization data of series of compound $\text{Co}_{1-x}\text{Mg}_x\text{Ta}_2\text{O}_6$, the powder samples were pressed into tiny pellets. These tiny pellets were then loaded in MPMS Quantum design instrument to measure the magnetization, temperature-magnetic field dependent measurements were performed. The magnetization was measured for the series of compounds from 2-300 K at zero field cool and field cool. The field cool measurements were done at 100 Oe and 1000 Oe respectively for all series of compounds.

The ZFC and FC arms of the $M(T)$ curve of CoTa_2O_6 are shown in figure 3.2 (a). The magnetization curves were recorded at an applied field, $H_{app}=1000$ Oe. A broad feature is present in the magnetization response around 15 K which shows no bifurcation between the ZFC and FC curves. Similarly, as a comparison, the FC $M(T)$ response of non-magnetic analogue MgTa_2O_6 which is purely paramagnetic, is also presented in the same graph. The enhancement of paramagnetic susceptibility seen at low temperatures could be due to the presence of minute defects or impurities that are polarized in the process of field cooling [13]. The broad magnetic anomaly that we have observed is also reported in the previous works on polycrystalline CoTa_2O_6 [23]. It is an unmistakable sign of the low dimensionality of the magnetic interaction in the Co- lattice. The change in slope that occurs at $T_N=6$ K is adjudged by the antiferromagnetic transition in the Co-lattice.

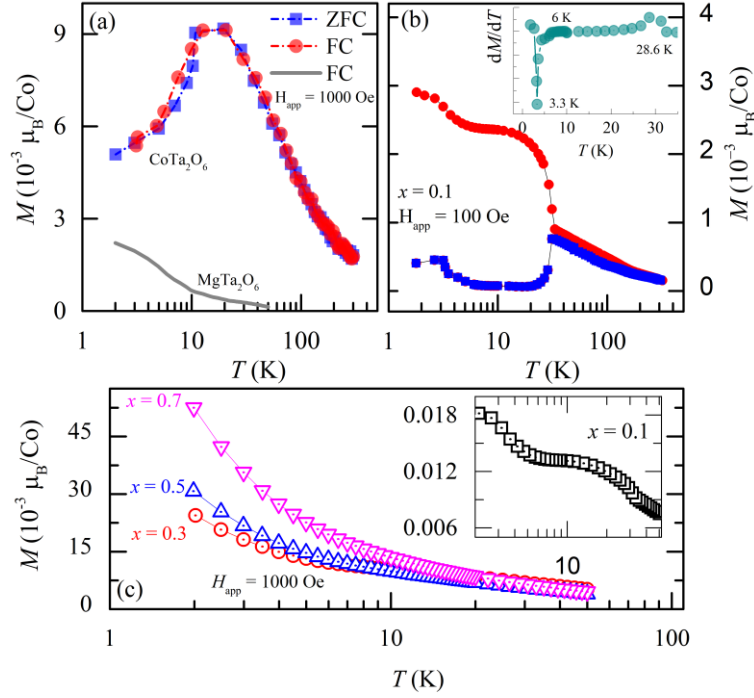


Figure 3.2: (a) The magnetization vs Temperature curve of CoTa_2O_6 in ZFC and FC protocols at $H_{\text{app}} = 1000$ Oe. The black marker shows the paramagnetic response of MgTa_2O_6 which is also represented in the same graph. (b) The ZFC and FC plots of at $H_{\text{app}} = 100$ Oe of $x = 0.1$ which showing a bifurcation at 30 K. The inserted graph of dM/dT show three anomalies in the case of $x = 0.1$. (c) An enhancement in magnetism are observed for $x = 0.5$, and 0.7 at low temperature. The inserted graph shows the FC curve of $x = 0.1$ at $H_{\text{app}} = 1000$ Oe.

3.3 CHARACTERIZATION USING CURIE-WEISS FIT AND LOW DIMENSIONAL MODELS

The Curies-Weiss fit was done to the high temperature region (150 K-320 K) of $M(T)$ for all compositions and obtained an average value of the effective moment as $4.9(2)\mu_B$ and $\theta_p = -50$ K. This value indicates that Co^{2+} in the $S=3/2$ state. However, if Co^{2+} is in a low-spin state a lower value in the range of $2 - 2.27\mu_B$ is observed [13]. The effective paramagnetic moment, Curie-Weiss temperature and the maximum magnetic moment obtained from the Curie-Weiss analysis is shown in the table II below.

Table II: Effective paramagnetic moment (μ_{eff}), Curie-Weiss temperature (θ_p), maximum magnetic moment (M_{max}), Lande g-factor, and Ising and Bonner-Fisher fit exchange parameter J_{nn}^I (K) and J_{nn}^{BF} (K) are shown in the table.

	μ_{eff} (μ_B/Co)	θ_p (K)	M_{max} (μ_B/Co)	G	J_{nn}^I (K)	J_{nn}^{BF} (K)
x = 0.0	4.9(2)	-50(2)	0.45	2.7(1)	-24	-15
x = 0.1	4.8(2)	-18(1)	0.54	3.3(2)	-25	-18
x = 0.3	4.3(3)	-27(2)	0.52	2.3(3)	-21	-16
x = 0.5	1.1(2)	-13(1)	0.53	1.9(3)	-18	-13
x = 0.7	2.9(3)	-25(2)	0.75	1.4(2)	-43	-10

The minimum value of effective moment was seen for $x = 0.5$ and is slightly increases for $x = 0.7$. It is very hard to explain the cause: however, the anomalies seen at seen at lattice parameter for $x = 0.5$ and $x = 0.7$ may be related to it. Another possibility can be the transformation of part of cobalt ions into low spin state [13]. The ZFC and FC curves of $M(T)$ of $x = 0.1$ recorded at $H_{\text{app}} = 100$ Oe is presented in the figure 3.2(b). Remarkable irreversibility is seen in the ZFC and FC arms of the magnetization, where bifurcation happens at $T_N=28.6$ K. Further anomalies are seen for $x = 0.1$ at $T_{N2} = 6\text{K}$ and $T_{N3} = 3.3$ K. The exact value of temperature was determined using derivative of magnetization with respect to temperature, dM/dT , which is also seen in the inserted figure 3.2(b). To our best knowledge, these anomalies were reported for the first time for $x = 0.1$ compound. No thermal hysteresis between the FC-warming and FC-cooling curves was observed, thereby ruling out any first order effect due to structural or magnetic disorder in the system. With the application of 1000 Oe, the anomalies are seen to smoothen out, however, broad features were seen to remains. From the table II the effective moment and the Curie-Weiss temperature are reduced compared to the $x = 0$

compound. However, predominant antiferromagnetic response is retained. As the Mg-content is increased further, the magnetic anomalies present in the $x = 0$ and $x = 0.1$ compositions vanish for $x = 0.3, 0.5$, and 0.7 which retain a paramagnetic -like response down to 2 K. The progressive enhancement of magnetization at low temperature with the increase in Mg-content. With progressive increase of Mg in the Co lattice, the antiferromagnetism is destabilized along the chains giving way to ferromagnetic clusters [13].

The broad peak in the magnetization as seen the figure 3.2 (a) is reminiscent of low dimensional (i.e. 1 dimensional spin chains) spin compounds. We analyzed magnetization data by using two models (a) Bronner-Fisher and (b) Ising model. We used Bronner-Fisher model as our first approach. The expression for magnetic susceptibility modeled by Bronner-Fisher is given by,

$$\chi_{BF} = \frac{Ng^2\mu_B^2}{k_B T} \left[\frac{0.25 + 0.14995 x + 0.30094 x^2}{1 + 1.9862 x + 0.68854 x^2 + 6.0626 x^3} \right] \quad (3.1)$$

Where N is the number of moles, g is the Lande g factor, μ_B is the Bohr magneton, and $x = \frac{|J|}{k_B T}$. The curve obtained after Bonner-Fisher fitting is shown in figure 3.3 (a-c). It is shown by solid blue line for $x = 0, 0.1$, and 0.7 respectively.

The next approach we used was modified Ising model. This approach well accounted the magnetic susceptibility of the single crystal of CoTa_2O_6 for $S=1/2$ dimers. We adopted spin-half expression for $S = 3/2$ in the case of Co^{2+} as follows,

$$\chi_I = \xi \left[\frac{e^{\frac{3J}{k_B T}} \left(2 + e^{\frac{2J}{k_B T}} + 8e^{\frac{3J}{k_B T}} + 9e^{\frac{6J}{k_B T}} \right)}{1 + 2e^{\frac{3J}{k_B T}} + e^{\frac{4J}{k_B T}} + 2e^{\frac{6J}{k_B T}} + e^{\frac{9J}{k_B T}}} \right] \quad (3.2)$$

Where $\xi = \frac{Ng^2\mu_B^2}{2k_B T}$. The figure 3.3 (a-c) shows the fit to the magnetic susceptibility for $\text{Co}_{1-x}\text{Mg}_x\text{Ta}_2\text{O}_6$, using the modified Ising model shown by green solid line. The quality of the fit

looks very good and for $x = 0$ i.e. CoTa_2O_6 , we get $g = 2.7(1)$ and $\frac{J}{k_B} = 24$ K, which are comparable to the values obtained for g_{\parallel} and J_{\parallel}/k_B in the case of single crystals of CoTa_2O_6 [23]. In the same figure 3.3 we have shown the fitting for the other compositions, $x = 0$, 0.1, and 0.7. The fitting like Bronner-Fisher and Ising models for low dimensional systems are consistently described for spin-half systems. The extension of these models does not exist for high-S systems. Therefore, we used a similar approach used by author A.B Christian *et al* [23]. The fit parameters obtained from the analysis is shown in the table II.

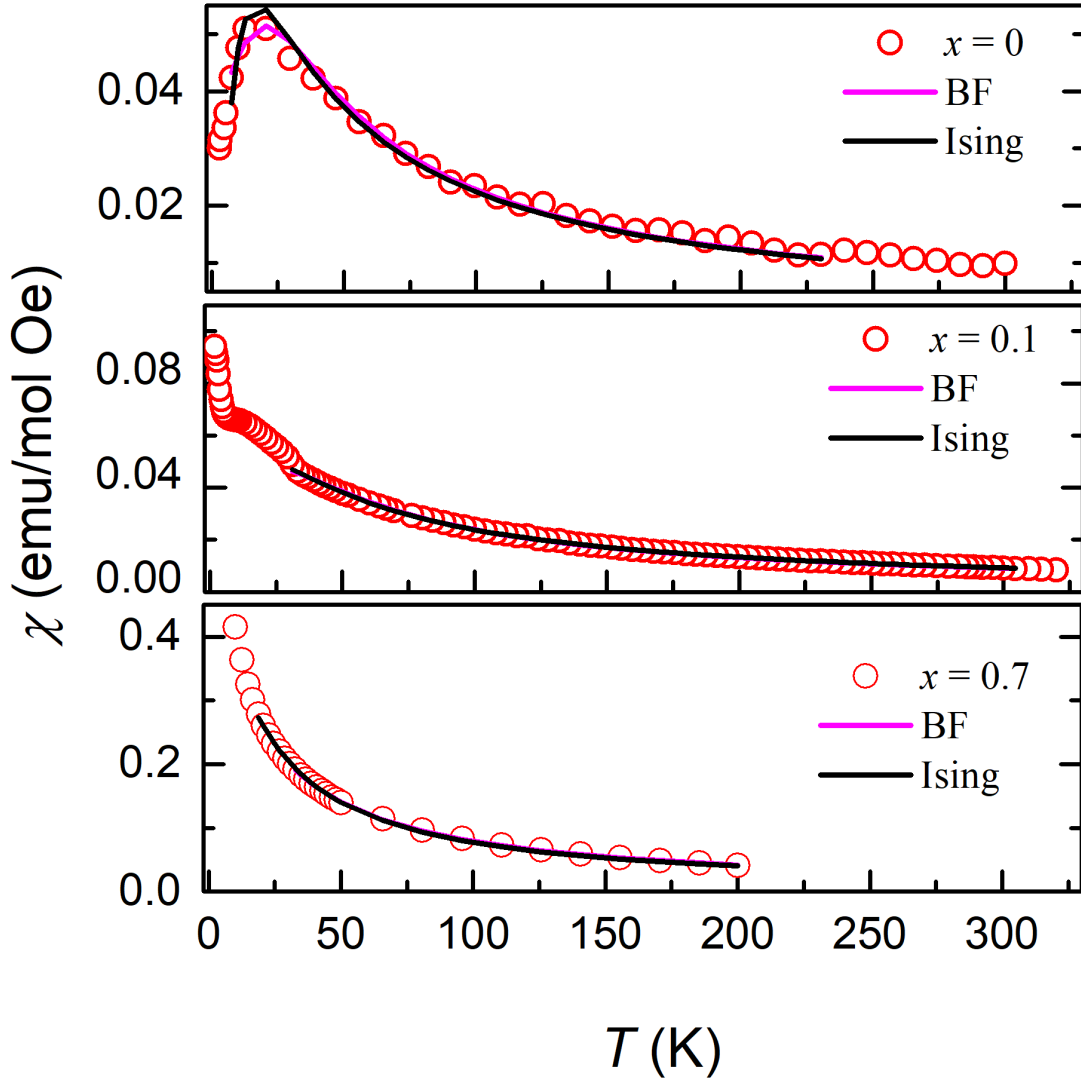


Figure 3.3. The magnetic susceptibility of $\text{Co}_{1-x}\text{Mg}_x\text{Ta}_2\text{O}_6$ compounds plotted in semi-log axis ($x = 0, 0.1$, and 0.7). The magnetic susceptibility data are fitted using Bonner-Fisher model which is represented by pink solid line and Ising model fit is shown by black solid line. The figures (a), (b), and (c) represents cases for $x = 0, 0.1$, and 0.7 respectively.

In the Figure 3.4, we present the isothermal magnetization curves $M(H)$, for the series of the compounds, i.e. $\text{Co}_{1-x}\text{Mg}_x\text{Ta}_2\text{O}_6$ at various temperature. The Figure 3.4 (a) represents the isothermal magnetization curve for $x = 0$ at 2 K, 10 K and 300 K. The $M(H)$ curve for $x = 0$ indicates its antiferromagnetic nature. The field-dependent transitions are presented for $x = 0$, at 2 K which are evident in the derivative curve of dM/dH . The critical fields $H_c = 2$ T and 5 T were observed. Similarly, the figure 3.4 (b) represents the isothermal magnetization curve for $x = 0.1$ at 2 K, 10 K and 300 K respectively. Similar to the previous case as in CoTa_2O_6 , the field-induced transition is obtained at $H_c = 1$ T for $x = 0.1$. As we increase the Mg-content the metamagnetic transition vanished in the series of the compound. The figure 3.4 (c) shows the magnetization curves for $x = 0.3, 0.5$, and 0.7 at constant temperature 2 K. We also observed weakly ferro-magnetic-like curvature for $x = 0.3, 0.5$, and 0.7 and sharp field induced transitions were absent. Our magnetization data provide the indication of weak ferromagnetism induced by the cluster of broken Ising spins in the chain like structure, which otherwise must show an antiferromagnetic structure [13].

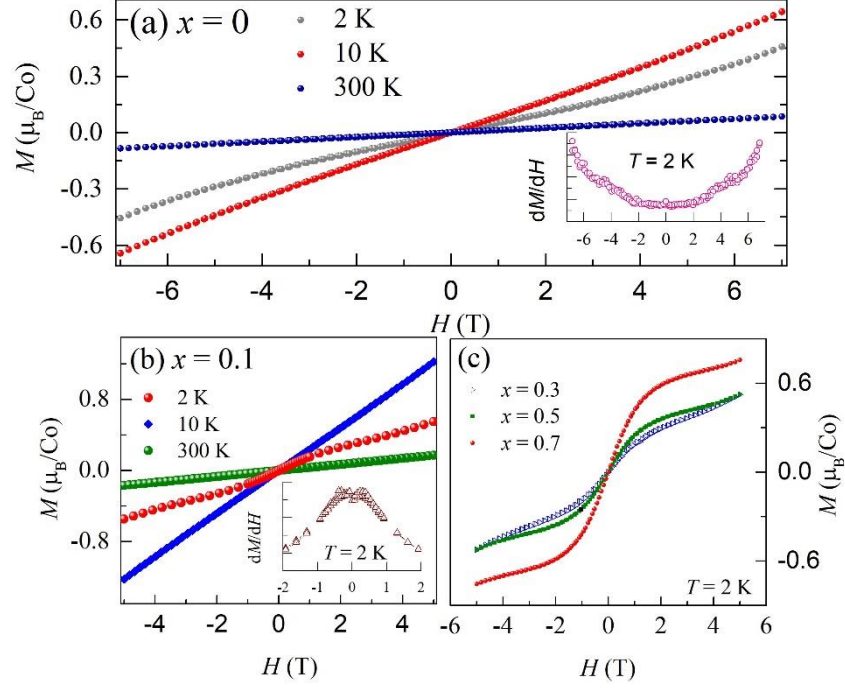


Figure 3.4: (a) The magnetization isotherm, $M(H)$, of CoTa_2O_6 at 2 K, 10 K, and 300 K. The insert graph shows the derivative, which reveals the field-induced transition at 2 T and 5 T. (b) shows the $M(H)$ of $x = 0.1$ at 2 K, 10 K, and 300 K. The insert graph shows a field induced transition present at 1 T at 2 K. (c) shows the $M(H)$ of $x = 0.3, 0.5$, and 0.7 at 2 K. Field-induced transitions are absent for these compositions

Chapter 4: Neutron Diffraction and Specific Heat of $\text{Co}_{1-x}\text{Mg}_x\text{Ta}_2\text{O}_6$

The magnetic properties of the $\text{Co}_{1-x}\text{Mg}_x\text{Ta}_2\text{O}_6$ series of compounds presented in the previous chapter were based on bulk magnetization measurements. These measurements proved that CoTa_2O_6 and the Mg-doped compositions did present significant short-range magnetic order at low temperature. This was evident from the broad feature in magnetization in the case of CoTa_2O_6 but was not so evident in the higher Mg-doped compositions as they did not present any broad features in magnetization. In order to understand the nature of magnetism, it is then important to study the magnetic and nuclear structure using microscopic probes. In this chapter we present the results from neutron diffraction experiments on $\text{Co}_{1-x}\text{Mg}_x\text{Ta}_2\text{O}_6$.

Neutron diffraction data on $\text{Co}_{1-x}\text{Mg}_x\text{Ta}_2\text{O}_6$ were collected using a high-resolution neutron powder diffractometer (PSD) at University of Missouri Research Reactor (MURR). For elastic neutron diffraction pure phased sample of CoTa_2O_6 and its derivatives about 4 g were prepared. For each compound, two sets of data were taken: at 11.1 K and at 295 K. Phase-pure sample of CoTa_2O_6 and its derivatives were loaded in a thin vanadium can which was then kept in an Al holder purged and filled with Helium. Neutrons of wavelength 1.485 \AA were employed for the elastic neutron diffraction. These diffraction data were collected over an angular range from 5° to 105° with step size of 0.05° . The background of the collected data was subtracted before we proceed it for the Rietveld analysis to probe magnetic structure. The whole refinement was done using Full-Prof suite based on the space group $P4_2/mnm$.

4.1 NEUTRON POWER DIFFRACTION

The Figure 4.1(a) shows the neutron powder diffraction for $x = 0, 0.3$, and 0.7 at room temperature, respectively. The crystal structure of CoTa_2O_6 i.e. $x = 0$, is well-studied in past [24]. CoTa_2O_6 has Co^{2+} and Ta^{5+} cations, which are surrounded by O^{2-} octahedra, and the

adjacent Co-O planes ($z = 0$ and $z = 1/2$) are separated by two TaO planes. The lattice parameters obtained from neutron diffraction of CoTa_2O_6 are comparable to earlier literature report [25].

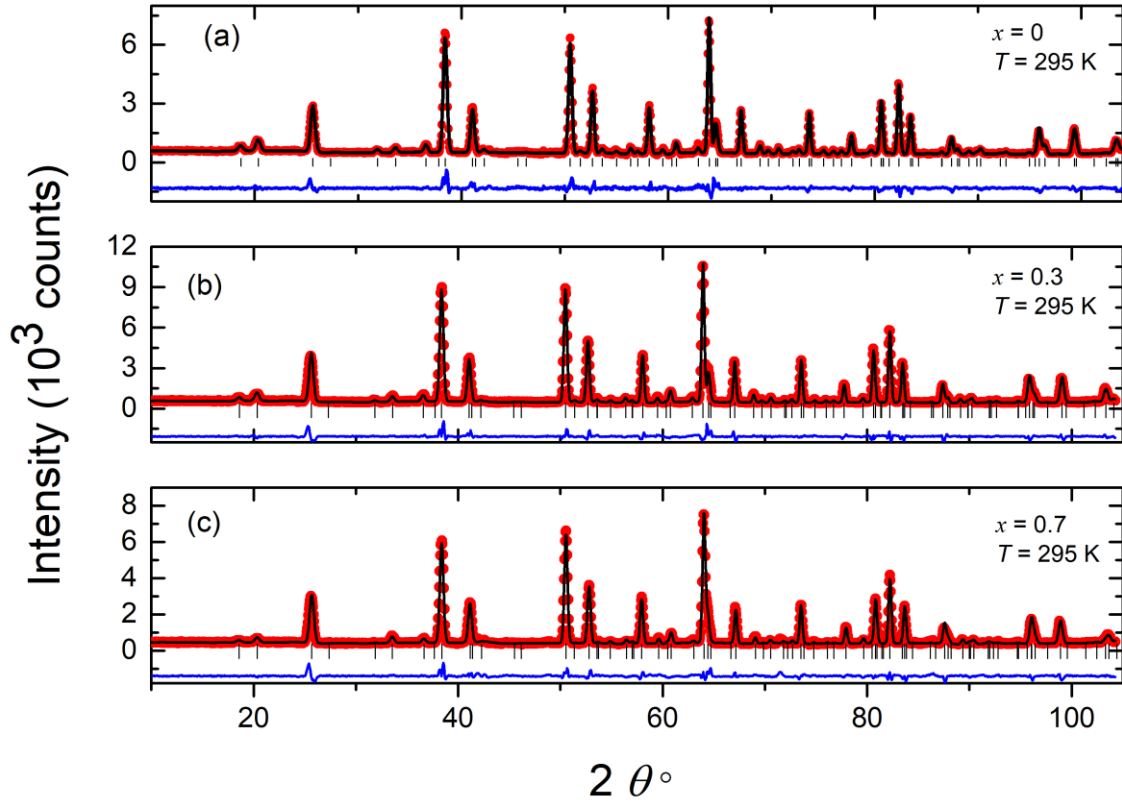


Figure 4.1: The neutron diffraction pattern for $x = 0, 0.3$, and 0.7 at $T = 295$ K. The red color represents, experimental data and the black solid line represents the Rietveld fit assuming the trirutile structure in $P4_2/mnm$ patterns. The difference patterns are shown in blue color and the green vertical tick marks represents the Bragg peaks. It is clear that all the compositions crystalline in tetragonal trirutile structure at room temperature.

The atomic position and refined lattice parameters for $x = 0, 0.3$, and 0.7 are presented in table III. Similarly, the Co – O bond distances and the O – Co – O bond angles for CoTa_2O_6 are presented in table III.

Table III: The atomic position and lattice parameters for the composition $x = 0, 0.3$, and 0.7 at temperature 295 K.

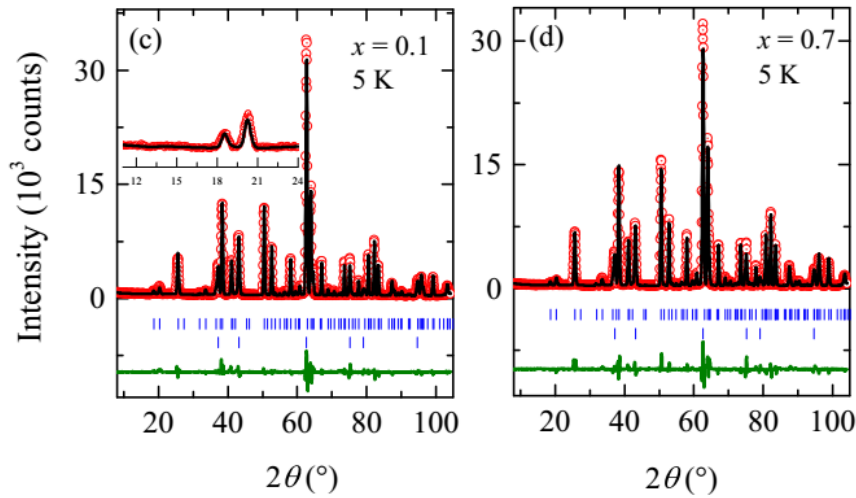
	Atom	x	y	z
$x = 0$	Co (2a)	0.0000	0.0000	0.0000
	Ta (4e)	0.0000	0.0000	0.3300
	O (4f)	0.3107	0.3107	0.0000
	O (8j)	0.2958	0.2958	0.3232
$x = 0.3$	Co (2a)	0.0000	0.0000	0.0000
	Mg (2a)	0.0000	0.0000	0.0000
	Ta (4e)	0.0000	0.0000	0.3296
	O (4f)	0.3137	0.3137	0.0000
	O (8j)	0.2953	0.2953	0.3243
$x = 0.7$	Co (2a)	0.0000	0.0000	0.0000
	Mg (2a)	0.0000	0.0000	0.0000
	Ta (4f)	0.0000	0.0000	0.3313
	O (4f)	0.3160	0.3160	0.0000
	O (8j)	0.2959	0.2959	0.3246
	c (Å)	b (Å)	c (Å)	T (K)
$x = 0$	4.7382	4.7382	9.1795	295
$x = 0.3$	4.7318	4.7318	9.1831	295
$x = 0.7$	4.7223	4.7223	9.1951	295

Table IV: Bond distance and bond angles for CoTa_2O_6

x	Co-O ₁ (Å)	Co-O ₂ (Å)	O ₂ -Co-O ₂ (degree)
0	2.0801	2.1196	80.297

0.3	2.0995	2.1162	80.652
0.7	2.1317	2.1073	80.688

The refined lattice parameter of CoTa_2O_6 at $T = 295$ K is comparable to the value reported in a structural report [25]. No structural phase transformation was observed in CoTa_2O_6 as a function of temperature down to 5 K or as a function of composition, x , in the case of $\text{Co}_{1-x}\text{Mg}_x\text{Ta}_2\text{O}_6$. The x -dependence of both a and c showed a weak anomaly at $x = 0.5$ which was reflected in the bond parameters as well. The most recent report on the neutron diffraction study of CoTa_2O_6 reports on a polycrystalline sample with impurities, CoO and Ta_2O_5 [20]. Though the crystal structure is refined in the $P 4_2/\text{mm}$ space group, the lattice constants reported ($a = 4.715(9)$ Å, and $c = 9.127(6)$ Å at 1.5 K) are different from the values obtained in the present work but at 5 K. With the reduction in temperature to 5 K, additional Bragg peaks at $2\theta \approx 11.3^\circ$, 14.2° , 11.3° , 17° and 19° are observed in the neutron powder diffraction pattern. These Bragg peaks are the indication that magnetic long-range order develops in CoTa_2O_6 below the $T_N = 6.2$ K. Further analysis is required to model the magnetic structure from the experimentally observed



neutron diffraction data. This thesis does not present the data analysis pertaining to the magnetic structure determination.

Figure 4.2: The neutron powder diffraction patterns obtained for $x = 0.1$ and 0.7 at 5 K are presented in Figure (c) and (d) respectively. The low-angle region of the pattern is shown magnified in (c) to clearly show that the magnetic Bragg peaks are absent even with Mg-dilution of 10%.

The macroscopic magnetization on the $x = 0.1$ composition by some of us [13] revealed anomalies in the temperature dependence of magnetization at low temperatures. The present results obtained through neutron diffraction confirms that the magnetism in CoTa_2O_6 is completely suppressed upon increasing the concentration of Mg by 10%. The neutron diffraction patterns of $x = 0.3, 0.5$ and 0.7 at 295 K and 5 K are similar to that of $x = 0.1$ confirming the absence of long-range magnetic ordering in $\text{Co}_{1-x}\text{Mg}_x\text{Ta}_2\text{O}_6$ for $x > 0.1$. The current results align well with the previous preliminary bulk magnetization data [13] except for an enhancement of ferromagnetic correlations found in the heavily doped composition ($x = 0.7$), however, in external fields. We do not observe experimental indications of diffuse magnetic order in any of the $\text{Co}_{1-x}\text{Mg}_x\text{Ta}_2\text{O}_6$ compositions.

4.2 SPECIFIC HEAT

The specific heat, $C_p(T)$, of CoTa_2O_6 obtained under the application of 0 T, 5 T and 7 T is presented in Figure 4.3(a). The $C_p(T)$ of the non-magnetic analogue compound MgTa_2O_6 is also plotted in (a). In the case of CoTa_2O_6 , a sharp λ -like transition is present at $T_N = 6.2$ K. External magnetic fields up to 7 T have negligible effect on the peak at T_N . An enhancement of $C_p(T)$ at $T < T_N$ is noticeable in the presence of external magnetic field. This may be compared to the weak enhancement of ferromagnetism previously observed in $x = 0.7$. For the $x = 0.1$ composition, a broad transition is observed in the specific heat. Previous magnetization results on the same composition had shown multiple magnetic anomalies below 28 K in low applied fields which smoothed into a broad transition at higher applied field. From the present specific heat data, it is clear that the anomalies in magnetization are related to magnetic clusters of probably short-range ordered regions which were smoothed under the application of external

magnetic field. Figure 4.3 (b) shows the plot of $C_p(T)$ versus temperature of all $\text{Co}_{1-x}\text{Mg}_x\text{Ta}_2\text{O}_6$ compositions studied in the present work. It is clear that with increasing Mg content, the magnetic transition at T_N is suppressed. For the $x = 0.1$ and 0.3 cases the transition broadens. By taking the derivative, dC_p/dT , we determined the transition temperatures for the $x = 0.1$ and 0.3 compounds. For the $x = 0.1$, anomalies in dC_p/dT are present at 4.9 K and 3.2 K (see the inset of (a)), whereas for the $x = 0.3$ case, at 4.5 K. The specific heat anomalies in (dC_p/dT) seen in the $x = 0.1$ case matches well with the results that we observed in magnetization earlier. In the inset of panel (b), the $C_p(T)$ of the $x = 0.5$ compound in 0 T and 7 T are plotted together. It can be seen that with the application of magnetic field, there is a slight enhancement in the specific heat below the T_N . In order to obtain the magnetic contribution, $C_m(T)$ towards total specific heat, we subtracted the $C_p(T)$ of MgTa_2O_6 from that of CoTa_2O_6 . The $C_m(T)$ of CoTa_2O_6 is presented in Fig 4.3 (a) which presents a sharp λ -like transition at $T_N = 6.2$ K. The Co atoms in CoTa_2O_6 have been treated as a square net of Ising spins and specific heat studied under that assumption. We have modeled the specific heat of Ising net of spins which is represented in (a) as a solid line. The $C_m(T)$ of the other compositions in the $\text{Co}_{1-x}\text{Mg}_x\text{Ta}_2\text{O}_6$ series are shown in the panel (b) of the figure. Evidently, the magnetic contribution to the specific heat decreases with increasing Mg content. The magnetic entropy that is obtained using $S_m = \int_0^T \frac{dC_m}{T} dT$, is plotted for all compositions in (c). Only 6% of the total spin-only entropy of $R \ln(2S + 1)$ ($S = 3/2$ and R is the universal gas constant) is released close to the T_N . Very low magnetic entropy is observed close to the magnetic ordering temperature indicating that significant spin fluctuations exist above the T_N . Similar conclusions were arrived at in the case of CoSb_2O_6 [23]. The low temperature specific heat of $\text{Co}_{1-x}\text{Mg}_x\text{Ta}_2\text{O}_6$ was analyzed using the expression, $C_m(T) = \gamma T + \beta T$. The fit parameters and the values of Debye temperature estimated for the different compositions are given in Table IV. The Debye temperature was estimated using the equation, $\theta_D = 12\pi^4 R / 5\beta$, where p is the number of atoms in the unit cell and R is the universal gas constant. The values of γ shows a gradual decrease as a function of composition, x ; whereas the β

values show an anomaly for $x = 0.5$. The value of γ that is observed in CoTa_2O_6 lies intermediate with the values of 203 mJ/mol K^2 for CoSb_2O_6 and 58.7 mJ/mol K^2 for CuSb_2O_6 [23].

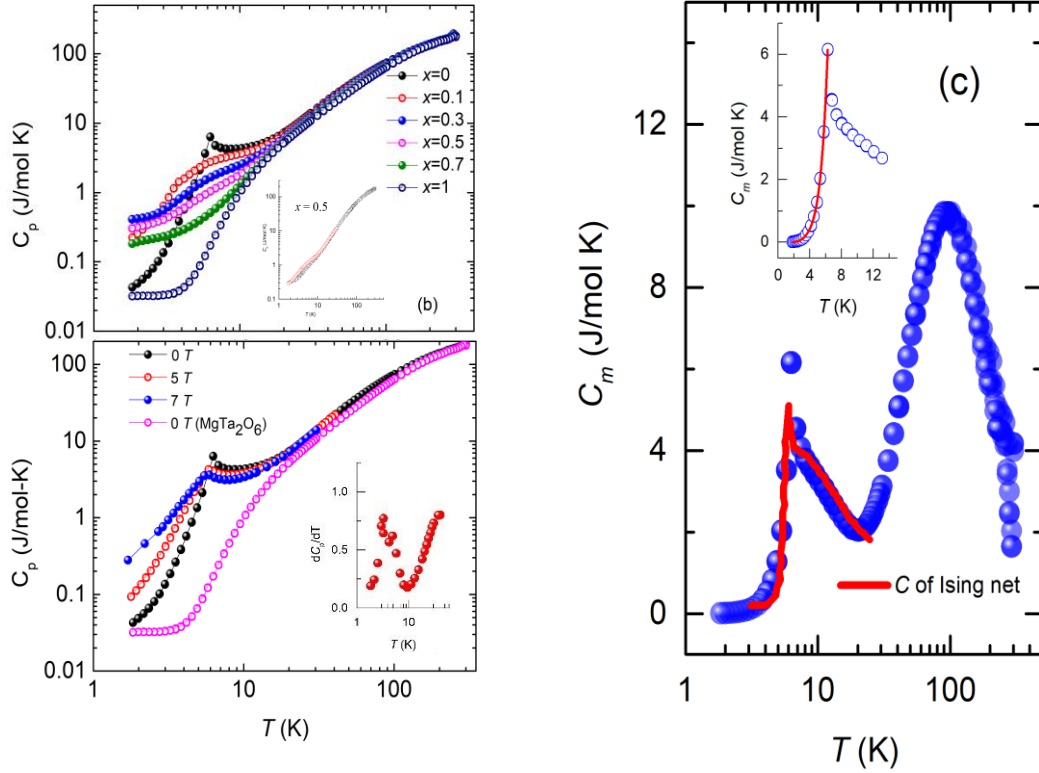


Figure 4.3: (a) Represents specific heat capacity for $x = 0$ at 0 T, 5 T, and 7 T. C_p of $x = 1$ so shown in same figure with pink color at 0 T, for comparison. The insert graph represents dC_p/dT for $x = 0.1$. Figure (b) represents the specific heat capacity for $x = 0, 0.1, 0.3, 0.5, 0.7$, and 1 at 0 T and the insert graph shows the C_p of $x = 0.5$ at 0 T and 7 T. Figure (c) represents Ising fit (red solid line) of magnetic specific heat for $x = 0$, in zero field.

The Ising nature of these compounds might point to the fact that the γ term signifies the magnetic excitations from the local magnetic order. The magnetic specific heat in the temperature range below T_N could be modeled using the expression, [23]

$$C_m(T) = A_1 T \exp(-\Delta_1/k_B T) + A_2 T^3 \exp(-\Delta_2/k_B T) \quad (3.3)$$

where, A_1 and A_2 are constants, Δ_1 and Δ_2 are the energy gap values. The second term is the familiar magnon term for an antiferromagnet with a gap in their excitation spectrum. A fit using this expression to the C_m of CoTa_2O_6 is shown in the inset of Fig 4 (a) using the red solid line. From the fit, $A_1 = 2.3(2)$, $A_2 = 5.7(7)$, $\Delta_1/k_B = 12.6(4)$ K and $\Delta_2/k_B = 36.5(9)$ K are obtained. As a comparison, 1.49 K and 33 K respectively were obtained for CoSb_2O_6 .

Table IV: The parameters exacted from the analysis of low temperature specific heat of $\text{Co}_{1-x}\text{Mg}_x\text{Ta}_2\text{O}_6$

x	γ (mJ/mol K ²)	β (mJ/mol K ²)	θ_D (K)
0	80.4(1)	0.0241(5)	892
0.1	55.4(3)	0.0254(3)	867
0.3	28.7(3)	0.0299(5)	829
0.5	13.3(7)	0.0191(7)	963
0.7	4.4(1)	0.0211(5)	931

Conclusion

We have synthesized high quality and pure phases of trirutile CoTa_2O_6 and its derivative by doping Co with Mg, $\text{Co}_{1-x}\text{Mg}_x\text{Ta}_2\text{O}_6$. The magnetic properties of CoTa_2O_6 shows features of low dimensional magnetism via broad features in magnetization. However, the specific heat shows a sharp peak at the transition which is not affected much by magnetic fields up to 7 T. The short-range magnetic contribution is seen as a broad peak in magnetization and specific heat at around 15 K. Our analysis of magnetic properties using models pertaining to low dimensional magnetism failed at obtaining a conclusive picture regarding if the spins are Ising or Heisenberg. Using neutron diffraction experiments we confirm the trirutile phase of the synthesized compounds. Preliminary magnetic structure determination using neutron data points towards a magnetic structure which deviates from 2D type. With the introduction of Mg in CoTa_2O_6 , the broad features in magnetization disappears. However, in the magnetization response, we see ferromagnetic features are slightly enhanced when Mg doping is increased to 70%. The present work indicates that CoTa_2O_6 has inherent magnetic short-range order that might be interesting to investigate using inelastic neutron scattering experiments. This preliminary work sets the stage for future experimental work on single crystals of CoTa_2O_6 .

References

- [1] N. D. Mermin and H. Wagner, Phys. Rev. Lett. **17**, 1307 (1966).
- [2] E. J. Kinast, C. A. dos Santos, D. Schmitt, O. Isnard, M. A. Gusmão, and J. B. M. da Cunha, J. Alloys Compd. **491**, 41 (2010).
- [3] R. Kremer, J. Greedan, E. Gmelin, W. Dai, M. White, and S. Eicher, J. Phys. Colloq. **6**, 6 (1988).
- [4] M. Takano and T. Takada, Mater. Res. Bull. **5**, 449 (1970).
- [5] K. Momma and F. Izumi, J. Appl. Crystallogr. **44**, 1272 (2011).
- [6] A. B. Christian, S. H. Masunaga, A. T. Schye, A. Rebello, J. J. Neumeier, and Y. Yu, **90**, 1 (2014).
- [7] J. M. Law, H. J. Koo, M. H. Whangbo, E. Brücher, V. Pomjakushin, and R. K. Kremer, Phys. Rev. B - Condens. Matter Mater. Phys. **89**, 4 (2014).
- [8] D. T. Maimone, A. B. Christian, J. J. Neumeier, and E. Granado, Phys. Rev. B **97**, 1 (2018).
- [9] A. B. Christian, A. T. Schye, K. O. White, and J. J. Neumeier, J. Phys. Condens. Matter **30**, (2018).
- [10] N. Prasai, A. Rebello, A. B. Christian, J. J. Neumeier, and J. L. Cohn, Phys. Rev. B - Condens. Matter Mater. Phys. **91**, (2015).
- [11] E. J. Kinast, V. Antonietti, D. Schmitt, O. Isnard, J. B. M. da Cunha, M. A. Gusmão, and C. A. dos Santos, Phys. Rev. Lett. **91**, 197208 (2003).
- [12] R. Kremer, J. Greedan, E. Gmelin, W. Dai, M. White, S. Eicher, and K. Lushington, J. Phys. Colloq. **49**, C8 (1988).
- [13] R. Baral, H. S. Fierro, L. M. Martinez, S. R. Singamaneni, and H. S. Nair, J. Appl. Phys. **125**, 033904 (2019).
- [14] C. Kittel, *Introduction to Solid State Physics*, 7th ed. (Wiley, New York, 1996).
- [15] Anthony R West, *Solid State Chemistry and Its Applications*, 2nd ed. (Wiley, 2014).
- [16] T. Heitmann and W. Montfrooij, *Practical Neutron Scattering at a Steady State Source*, 1st ed. (Mizzou Media - University BookStores, Missouri, 2012).
- [17] E. H. Kisi and C. J. Howard, *Applications of Neutron Powder Diffraction* (Oxford University

- Press, New York, 2008).
- [18] F. Fernandez-Alonso and D. L. Price, *Neutron Scattering : Fundamentals* (Academic Press, Amsterdam, 2013).
 - [19] A.-J. Dianoux and L. Gerry, *NEUTRON DATA BOOKLET*, 2nd ed. (OCP Science, 2003).
 - [20] G. Will, *Powder Diffraction: The Rietveld Method and the Two Stage Method to Determine and Refine Crystal Structures from Powder Diffraction Data* (New York, 2006).
 - [21] O. Master, S. In, and C. Matter, *Magnetism in Condensed Matter - Stephen Blundell.Pdf* (Oxford University Press, New York, 2001).
 - [22] E. S. R. Gopal, *Specific Heats at Low Temperatures*, 1st ed. (Plenum Press, New York, 1966).
 - [23] A. B. Christian, A. Rebello, M. G. Smith, and J. J. Neumeier, *Physical Rev. B* **92**, 174425 (2015).
 - [24] V. Antonietti, E. J. Kinast, L. I. Zawislak, J. B. M. Da Cunha, and C. A. Dos Santos, *J. Phys. Chem. Solids* **62**, 1239 (2001).
 - [25] J. N. Reimers, J. E. Greedan, C. V Stager, and R. Kremer, *J. Solid State Chem.* **83**, 20 (1989).

Vita

My name is Raju Baral. I did my undergraduate and graduate study in physics from Tribhuvan University, Nepal. As soon as I completed my graduate study from Tribhuvan University, I joined Bagmati College as a physics lecture, where I taught physics for seven years. In August 2017, I joined The University of Texas at El Paso (UTEP) for my master's in physics and started working in **Dr. Nair's** lab. During my studies in UTEP, I got an opportunity to a teaching assistant and I also worked as a research assistant during both summer sessions. During my two years master's program in UTEP, I was able to present my research work in various conferences like Gordon Research and MRS conferences. With the support and guideline of **Dr. Nair**, I was able to publish two papers, one of which was on my thesis. For this I would like to thank my advisor and also like to thank department of physics UTEP for providing me the travel funds for both conferences.

Permanent address: Kaseri, Arwabijaya 04
 Kaski, Nepal

This thesis/dissertation was typed by Raju Baral.